
This EarthArXiv preprint is a non-peer reviewed version of the manuscript submitted to AMS Artificial Intelligence for the Earth Systems (AIES). Copyright may be transferred without further notice.

Sub-seasonal Prediction of Central European Summer Heatwaves with Linear and Random Forest Machine Learning Models

Elizabeth Weirich Benet,^a Maria Pyrina,^a Bernat Jiménez-Esteve,^a Ernest Fraenkel,^b Judah Cohen,^{c,d} and Daniela I.V. Domeisen^{e,a}

^a *Institute for Atmospheric and Climate Science, ETH Zürich, Zürich, Switzerland*

^b *Department of Biological Engineering, MIT, Cambridge, USA*

^c *Atmospheric and Environmental Research (AER), Lexington, USA*

^d *Department of Civil and Environmental Engineering, MIT, Cambridge, USA*

^e *Institute of Earth Surface Dynamics, Université de Lausanne, Lausanne, Switzerland*

Corresponding author: Elizabeth Weirich Benet (weiriche@ethz.ch) and Daniela I.V. Domeisen (daniela.domeisen@env.ethz.ch)

16 ABSTRACT: Heatwaves are extreme near-surface temperature events that can have substantial
17 impacts on ecosystems and society. Early Warning Systems help to reduce these impacts by helping
18 communities prepare for hazardous climate-related events. However, state-of-the-art prediction
19 systems can often not make accurate forecasts of heatwaves more than two weeks in advance, which
20 are required for advance warnings. We therefore investigate the potential of statistical and machine
21 learning methods to understand and predict central European summer heatwaves on timescales of
22 several weeks. As a first step, we identify the most important regional atmospheric and surface
23 predictors based on previous studies and supported by a correlation analysis: 2-m air temperature,
24 500-hPa geopotential, precipitation, and soil moisture in central Europe, as well as Mediterranean
25 and North Atlantic sea surface temperatures, and the North Atlantic jet stream. Based on these
26 predictors, we apply machine learning methods to forecast two targets: summer temperature
27 anomalies and the probability of heatwaves for 1–6 weeks lead time at weekly resolution. For each
28 of these two target variables, we use both a linear and a random forest model. The performance
29 of these statistical models decays with lead time, as expected, but outperforms persistence and
30 climatology at all lead times. For lead times longer than two weeks, our machine learning models
31 compete with the ensemble mean of the European Centre for Medium-Range Weather Forecasts’
32 hindcast system. We thus show that machine learning can help improve sub-seasonal forecasts of
33 summer temperature anomalies and heatwaves.

34 SIGNIFICANCE STATEMENT: Heatwaves (prolonged extremely warm temperatures) cause
35 thousands of fatalities worldwide each year. These damaging events are becoming even more
36 severe with climate change. This study aims to improve advance predictions of summer heatwaves
37 in central Europe by using statistical and machine learning methods. Machine learning models
38 are shown to compete with conventional physics-based models for forecasting heatwaves more
39 than two weeks in advance. These early warnings can be used to activate effective and timely
40 response plans targeting vulnerable communities and regions, thereby reducing the damage caused
41 by heatwaves.

42 **1. Introduction**

43 A heatwave is an extended period of extremely hot weather relative to the expected local con-
44 ditions at that time of the year. These high temperatures can cause substantial damage to human
45 health, agriculture, infrastructure, and biodiversity (Barriopedro et al. 2011; Perkins 2015). Heat-
46 waves are among the most dangerous natural hazards (Basu 2002; Lowe et al. 2011), having caused
47 more than 166,000 deaths across the world between 1998 and 2017, including 70,000 fatalities
48 during the 2003 European heatwave (Wallemacq et al. 2018). Summer heatwaves are associated
49 with higher wet-bulb temperatures than winter heatwaves (Buzan and Huber 2020), resulting in
50 higher mortality (Huynen et al. 2001). In addition, the probability of other natural disasters, such
51 as wildfires, is higher during heatwaves (e.g., the 2020 Australian wildfires ignited amid a record-
52 breaking heatwave (Deb et al. 2020)). Furthermore, climate change leads to more extreme hot
53 weather (Barriopedro et al. 2011; Perkins 2015), and an increase in heatwave intensity, duration,
54 and frequency (Ford et al. 2018; Perkins and Alexander 2013; Perkins-Kirkpatrick and Lewis 2020;
55 Seneviratne et al. 2014).

56 Preparation for heatwaves is possible to a certain extent, for example through early warning sys-
57 tems (EWS) (Merz et al. 2020), which enable an effective and timely response targeting vulnerable
58 populations and regions. For instance, EWS help to determine when crops will need more irriga-
59 tion, when cooling centers must be set up, or when local hospitals must prepare for an additional
60 number of patients (Bassil and Cole 2010). Moreover, measures for heatwave preparedness on
61 the order of seasons to decades have to be taken by governments and municipalities (Casanueva
62 et al. 2019; Kotharkar and Ghosh 2022). Hence, the time needed to prepare for heatwaves is

63 often beyond the timescales of medium-range weather forecasts (up to two weeks) (de Perez et al.
64 2018). While forecasts on seasonal timescales show potential, a skill gap between two weeks and
65 seasonal timescales remains (Robertson et al. 2015; White et al. 2017). Alternative approaches
66 must therefore be explored to extend the lead time of skillful forecasts to sub-seasonal timescales
67 (two weeks to two months).

68 Central European heatwave predictability can be enhanced by a range of precursors, including
69 both local and remote drivers linked to European temperatures via teleconnections. Heatwaves
70 are generally associated with local persistent blocking anticyclones or upper-level ridges (Kautz
71 et al. 2022; Suarez-Gutierrez et al. 2020). The atmospheric circulation associated with these
72 persistent features exhibits predictability timescales of up to two weeks (Weyn et al. 2019; Zheng
73 and Frederiksen 2007). In turn, the latitude and speed of the North Atlantic (NA) jet stream, which
74 are influenced by the distribution of topography (Jiménez-Estevé and Domeisen 2022), affect the
75 occurrence and location of these atmospheric features and, hence, central European heatwaves
76 (Bladé et al. 2011; Oliveira et al. 2020). For instance, when the Summer East Atlantic (SEA)
77 pattern (i.e., the second dominant mode of summer low-frequency variability in the Euro-Atlantic
78 region) is in its positive phase, with low pressure west of the British Isles and high pressure to the
79 east, the weather tends to be unusually warm over Europe (Wulff et al. 2017). The SEA pattern
80 shows longer predictability timescales than local geopotential, on the order of 2–3 weeks (Vitart
81 2014; Zuo et al. 2016).

82 Cold sea surface temperature (SST) anomalies in the NA are also found to be present prior
83 to the onset of the most extreme European heat waves since 1980 (Duchez et al. 2016) (e.g.,
84 anomalously cold NA SSTs were key to the development of the 2015 European heatwave (Mecking
85 et al. 2019)). Moreover, northwestern Mediterranean (NWMED) SSTs are linked to temperatures
86 over the European continent due to their proximity and large heat capacity, acting as a heat buffer
87 for land temperatures (e.g., the 2003 European heatwave was connected to warm Mediterranean
88 SSTs) (Black et al. 2004). Since SST anomalies tend to be highly persistent, in extratropical
89 regions, weekly mean SST anomalies are associated with longer predictability of weeks to months
90 (Hu et al. 2012; Kumar and Zhu 2018).

91 Furthermore, precipitation is linked to surface air temperature via several mechanisms, including
92 changes in incoming solar radiation and surface sensible heat flux. Precipitation is characterized

93 by high-frequency variability and, thus, it is not expected to be predictable at lead times longer
94 than a few weeks (Li and Robertson 2015; Wheeler et al. 2016). Precipitation directly influences
95 soil moisture, which is another driver of summer heatwaves (Fischer et al. 2007). Dry soils (low
96 soil moisture) and warming reinforce each other through a positive feedback effect (Kolstad et al.
97 2017): Moist soils mostly cool through latent heat flux to the atmosphere, while dry soils emit
98 more sensible heat (Laguë et al. 2019) and hence heat up the atmosphere faster than moist soils.
99 This warmer atmosphere, in turn, results in even more dryness, closing the positive feedback loop
100 (Seneviratne et al. 2010). In addition, increased sensible heating can help maintain a blocking
101 anticyclone over land (Miller et al. 2021). Consequently, dry springs are more likely to be followed
102 by extremely high summertime temperatures (Mueller and Seneviratne 2012; Perkins 2015).

103 We here investigate whether the sub-seasonal forecasting accuracy of summer temperature
104 anomalies and heatwaves in central Europe (CE) can be improved by using linear and random
105 forest (RF) machine learning (ML) models based on these precursors. Other studies use ML and
106 deep learning (DL) to forecast temperature and heatwaves, targeting timescales different from sub-
107 seasonal (Khan et al. 2019; Kämäräinen et al. 2019; Pyrina et al. 2021) or North America instead
108 of CE (Chattopadhyay et al. 2020; Miller et al. 2021; Sobhani et al. 2018; Vijverberg et al. 2020).
109 Moreover, DL architectures successfully predict the onset of long-lasting extreme heatwaves in
110 France two weeks in advance (Jacques-Dumas et al. 2022) and yield increased predictability with
111 respect to the European Centre for Medium-Range Weather Forecasts (ECMWF) at lead times of
112 3–4 weeks (Lopez-Gomez et al. 2022), agreeing with the findings of the present study despite using
113 a different set of predictors. Finally, additional predictors are identified in a related study by using
114 explainable ML methods (van Straaten et al. 2022).

115 **2. Methods**

116 *a. Data*

117 1) PREDICTOR SELECTION

118 Seven atmospheric and surface predictors that are expected to be related to summer temperature
119 and heatwaves in CE based on previous studies (Section 1) and a correlation analysis (Section
120 3b1) are selected: 2-m air *temperature*, 500-hPa *geopotential*, *precipitation*, *soil moisture*, the
121 *SEA index*, *NWMED SST*, and *cold North Atlantic anomaly (CNA) SST*. Geopotential at the

122 500-hPa pressure level is used instead of sea-level pressure to avoid capturing the influence of high
123 surface temperatures on the local low-level surface pressure (Suarez-Gutierrez et al. 2020). The
124 following predictors were also evaluated but were not used, as they correlated only weakly with
125 2-m air *temperature*: deep soil moisture (28–289 cm underground), the Summer North Atlantic
126 Oscillation (i.e., the first dominant mode of summer low-frequency variability in the Euro-Atlantic
127 region), southeastern Mediterranean SST, Baltic SST, El Niño Southern Oscillation SST, the North
128 Atlantic SST index by Ossó et al. (2020), and the Pacific-Caribbean Dipole index by Wulff et al.
129 (2017). The seven selected predictors are considered in the extended summer season (MJJAS),
130 during the time period between 1 May 1981 and 30 September 2018. Technical details about these
131 predictors can be found in Table 1. Since both local predictors and remote teleconnections are
132 included, their locations are shown in Fig. 1 and their latitude-longitude coordinates are provided
133 in Table 2.

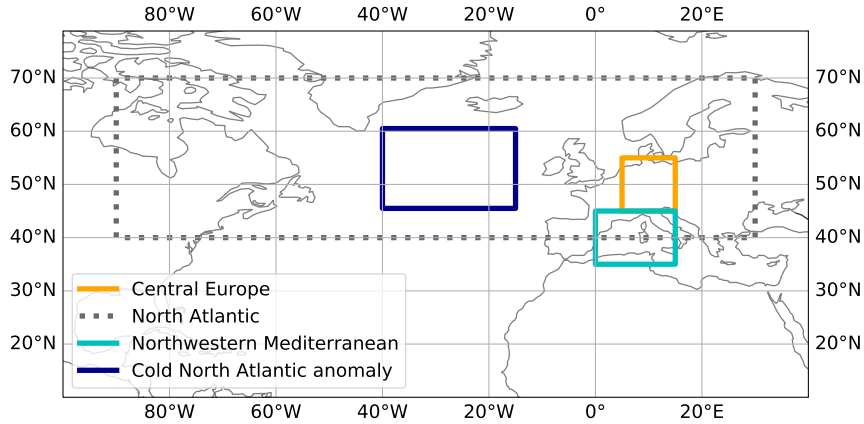
134 *Calculation of the SEA index* The changes in speed and location of the NA jet stream are included
135 in our set of predictors through the *SEA* index. First, the *SEA* pattern is calculated via principal
136 component analysis (PCA) (Storch and Zwiers 2003, chap. V), applied on the detrended 500-hPa
137 geopotential height anomalies over the NA box for the summer season (JJA). The *SEA* index
138 corresponds to the time-dependent coefficients (or PCA amplitudes) of the second PCA pattern
139 (Wulff et al. 2017). Then, the daily *SEA* index is calculated for the extended summer season
140 (MJJAS) by projecting the *SEA* pattern on the daily values of the 500-hPa geopotential height
141 anomalies from May to September and the obtained time series are normalised ($\mu = 0$, $\sigma = 1$).

154 2) DATA PREPROCESSING PIPELINE

155 First, we select latitude-longitude boxes for each physical magnitude and take either the arithmetic
156 mean of the area or perform PCA (Table 1) to obtain one-dimensional time series. The maximum
157 overlap period for the selected predictors is chosen as 1 May 1981 to 30 September 2018 (38
158 summers). We then detrend each time series by subtracting the linear trend. Detrending the data
159 removes linear long-term trends, which could be influenced by external climate forcing. Next, we
160 compute the daily climatology (x_{clim}), defined as the mean over the full time period for a particular
161 day of the year. We smooth the daily climatology by a centred 31-day rolling mean window.
162 We then compute the anomalies with respect to climatology as: $x_{\text{anom}} = x - x_{\text{clim}}$. This way, also

Predictor	Physical magnitude (units)	Source (Space, Time Res.)	Level	Box	Method
Temperature	2-m air temperature (°C)	E-OBS (0.25°, daily)	2 m a.g.	CE	avg
Geopotential	geopotential (m ² s ⁻²)	ERA-Interim (2.5°, daily)	500 hPa	CE	avg
Precipitation	rainfall (mm)	E-OBS (0.25°, daily)	surface	CE	avg
Soil moisture	volumetric soil water layer (m ³ m ⁻³)	ERA5-Land (2.5°, daily)	0–28 cm u.g.	CE	avg
SEA index	geopotential (m ² s ⁻²)	ERA-Interim (2.5°, daily)	500 hPa	NA	PCA
NWMED SST	sea surface temperature (°C)	HadISST (1°, monthly)	sea level	NWMED	avg
CNAA SST	sea surface temperature (°C)	HadISST (1°, monthly)	sea level	CNAA	avg

142 **TABLE 1. Properties of the predictors.** For each predictor, the name of the corresponding variable (physical
143 magnitude) as labeled in the dataset (source) is presented. We also indicate the temporal and spatial resolution
144 at which each variable was downloaded, the extracted vertical level, the selected spatial location, and the method
145 used to convert the three-dimensional time-latitude-longitude space into a one-dimensional time series. The soil
146 moisture (0–28 cm u.g.) is calculated as the average over the first two layers (layer one: 0–7 cm u.g. and layer two:
147 7–28 cm u.g.). The monthly sea surface temperature (SST) predictors are interpolated to daily time resolution.
148 Notation: Summer East Atlantic (SEA), northwestern Mediterranean (NWMED), cold North Atlantic anomaly
149 (CNAA), above ground (a.g.), and underground (u.g.).



150 **FIG. 1. Location of latitude-longitude boxes.** Used to define the location of the predictors shown in Table 1.
151 The latitude-longitude coordinates of the boxes are shown in Table 2.

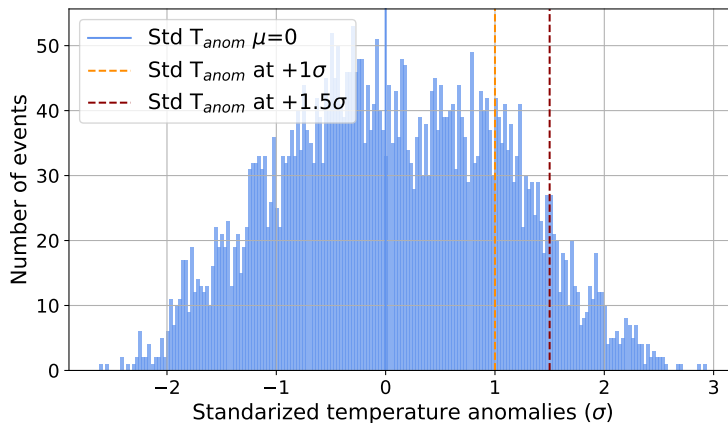
163 periodic changes due to seasonality are removed. Afterwards, to reduce the noise caused by natural
164 variability, which might lead to overfitted statistical models, these anomalies are smoothed out via
165 a 7-day centred rolling mean. Then, we standardize the predictors: $x_{\text{std anom}} = \frac{x_{\text{anom}}}{x_{\text{std}}}$, where $x_{\text{std anom}}$
166 are the standardized anomalies and x_{std} the standard deviation of the distribution of each predictor.
167 Furthermore, for each of the six prediction lead times (1–6 weeks), the predictors are provided to

Box	Latitude	Longitude
Central Europe (CE)	45°N–55°N	5°E–15°E
North Atlantic (NA)	40°N–70°N	90°W–30°E
Northwestern Mediterranean (NWMED)	35°N–45°N	0°–15°E
Cold North Atlantic anomaly (CNAА) (Duchez et al. 2016)	45°N–60°N	15°W–40°W

152 TABLE 2. **Coordinates of latitude-longitude boxes.** The boxes correspond to the location of the predictors of
153 Table 1 as seen in Fig. 1.

168 the ML models for the four weeks before initialization. For example, for a forecast at two weeks
169 lead time (meaning that we are using a statistical model initialized two weeks before the target
170 week for which we make the forecast), the *precipitation* from two, three, four, and five weeks before
171 the target week is used as a predictor by the ML models. Finally, since we want to investigate the
172 predictability of summer temperature, the extended summer months (MJJAS) are selected.

173 3) HEATWAVE INDEX DEFINITIONS



174 FIG. 2. **Histogram of temperature anomalies averaged over CE for the definition of heatwave indices.**
175 The blue bars correspond to the standardized ($\mu = 0$, $\sigma = 1$) temperature anomalies. The data is smoothed by a
176 7-day running mean (Section 2a2). The vertical blue line marks the mean ($\mu = 0$) of the distribution. The stippled
177 orange (red) line marks +1 (+1.5) standard deviations (σ) from the mean and is used to define heatwaves.

178 We define weekly heatwaves via a binary index: one for a heatwave week and zero, otherwise.
179 While there is no universal definition for heatwaves and a range of different indices are found
180 across the literature, percentile-based definitions are widely used (Perkins and Alexander 2013;
181 Perkins 2015; Perkins-Kirkpatrick and Lewis 2020; Spensberger et al. 2020). We use two different

182 heatwave definitions, thereby defining two independent classification problems: $+1\sigma$ for high and
 183 $+1.5\sigma$ for extremely high temperature anomalies (Fig. 2). The $+1\sigma$ weekly heatwave index is
 184 defined as one for the weekly mean temperature anomalies above one standard deviation (σ) (i.e.,
 185 to the right of the orange line in Fig. 2) and zero, otherwise. Analogously, the $+1.5\sigma$ weekly
 186 heatwave index is defined as one for the weekly mean temperature anomalies above 1.5 standard
 187 deviations (i.e., to the right of the red line in Fig. 2) and zero, otherwise. The number of heatwave
 188 and no-heatwave samples can be found in Table 3.

Weekly heatwave index	$+1\sigma$	$+1.5\sigma$
Absolute number of heatwave events	1,121	430
Absolute number of no-heatwave events	4,813	5,504
Percentage of heatwaves	18.89%	7.25%

189 **TABLE 3. Class imbalance.** Class distribution of the 5,934 samples in the extended summer (MJJAS) and the
 190 1981–2018 time period.

191 *b. Lead time*

192 We forecast at 1–6 weeks lead time. The statistical models are trained separately for each
 193 lead time and do not learn from each other. For instance, the two-weeks-lead-time forecast does
 194 not receive the one-week-lead-time forecast as an additional input. Moreover, since our data is
 195 averaged via a seven-day rolling mean (Section 2a2), weeks are labeled by their central day. A
 196 one-week-lead-time prediction leaves no gap between the days used to calculate the one-week-lag
 197 predictors and the days used to determine the target. For instance, the one-week-lead-time forecast
 198 run on June 4th (average over June 1st–June 7th) forecasts June 11th (average over June 8th–June
 199 14th). Similarly, a lead time of two weeks leaves a gap of seven unused days.

200 *c. Machine learning models*

201 For our study, we choose statistical models at the two extremes of the bias-variance tradeoff
 202 (Mehta et al. 2019). (1) The simpler linear models are prone to have high bias, meaning that the
 203 model will match the training set less closely. These models have a higher potential for under-
 204 fitting. Linear models, however, have low variance, meaning that the predictions of the model do

205 not fluctuate much with a change of dataset. Overall, these models are focused on the larger trends
 206 rather than on the complicated patterns of the training set. (2) By contrast, the more complex
 207 decision trees (DTs) are likely to overfit the data, but also to capture most of the relevant patterns.
 208 They tend to have high variance, but low bias. To mitigate the risk of DTs overfitting, we use RFs
 209 instead.

210 Two statistical models from each of these two families (1 and 2) are used for the regression and
 211 classification forecasts: ridge regressor (RR), ridge classifier (RC), random forest regressor (RFR),
 212 and random forest classifier (RFC). Moreover, the final forecasts by each model are the average of
 213 an ensemble of these ML models trained on slightly different samples (Section 2h).

214 1) LINEAR MODELS

215 Linear regression models forecast the target time series $\mathbf{y} = (y_t)$ as a linear combination of N
 216 predictor time series $\mathbf{x}_n = (x_{n,t})$:

$$\hat{\mathbf{y}}(\boldsymbol{\omega}, \mathbf{X}) = \omega_0 + \omega_1 \mathbf{x}_1 + \dots + \omega_N \mathbf{x}_N \quad (1)$$

217 where ω_0 is the intercept, ω_n ($0 < n \leq N$) are the regression coefficients, and $t \in [1, T]$ is the time
 218 step. The coefficients are chosen to minimize the residual sum of squares between the forecast ($\hat{\mathbf{y}}$)
 219 and the observed target (\mathbf{y}): $\min_{\boldsymbol{\omega}} \|\hat{\mathbf{y}} - \mathbf{y}\|$. Linear classification models first convert binary targets
 220 to $\{-1, 1\}$ and then treat the problem as a regression task. The forecast class corresponds to the sign
 221 of the regressor's forecast. We use Ridge regularization to control excessively fluctuating functions
 222 by adding an additional penalty term in the error function, such that the coefficients do not take
 223 extreme values (Hastie et al. 2009, chap. 3). Ridge shrinks the predictor coefficients based on the
 224 L2-norm ($\|\boldsymbol{\omega}\|_2 = \sqrt{\sum_{n=1}^N \omega_n^2}$). The loss function for minimization then becomes $\|\hat{\mathbf{y}} - \mathbf{y}\| + \alpha \|\boldsymbol{\omega}\|_2^2$,
 225 where the complexity parameter α is a hyper-parameter which controls the amount of shrinkage.

226 2) RANDOM FORESTS

227 A DT makes a recursive partition of the input space into rectangles, by selecting the predictor and
 228 the respective cutting point that discriminate best at each node. The resulting leaves correspond to
 229 a specific forecast value (regression) or to a probability of belonging to the positive class (binary
 230 classification). However, DTs have two key disadvantages: (1) Trees usually have high variance

231 due to their greedy split process, which implies that a small change in training data can result in
 232 significantly different splits. (2) Since the tree estimate is not smooth, DTs may not be appropriate
 233 when the underlying function is smooth (Khan et al. 2019). A more accurate and robust statistical
 234 model can be constructed by creating a random ensemble of DTs whose averaged prediction is
 235 more accurate than that of any individual tree. RFs use two sources of randomness while training:
 236 bagging and feature randomness (Breiman 2001). (1) Bagging (or bootstrap aggregation) consists
 237 in selecting a random subset of the training set with replacement –meaning that individual data
 238 points can be chosen more than once– to train each individual tree. (2) When splitting a node in a
 239 classical DT, all features are considered and the one that provides the greatest separation between
 240 observations is selected. In contrast, each individual tree in a RF can pick only from a random
 241 subset of features (Hastie et al. 2009, chap. 15). Finally, the mean or majority-vote forecast of all
 242 the regression or classification trees in the forest is selected as the final result, respectively. RFs
 243 are chosen over other tree-based algorithms since they are more interpretable (Rudin 2019) than
 244 gradient boosting and less prone to overfit than single DTs.

245 *d. Hyper-parameter optimization*

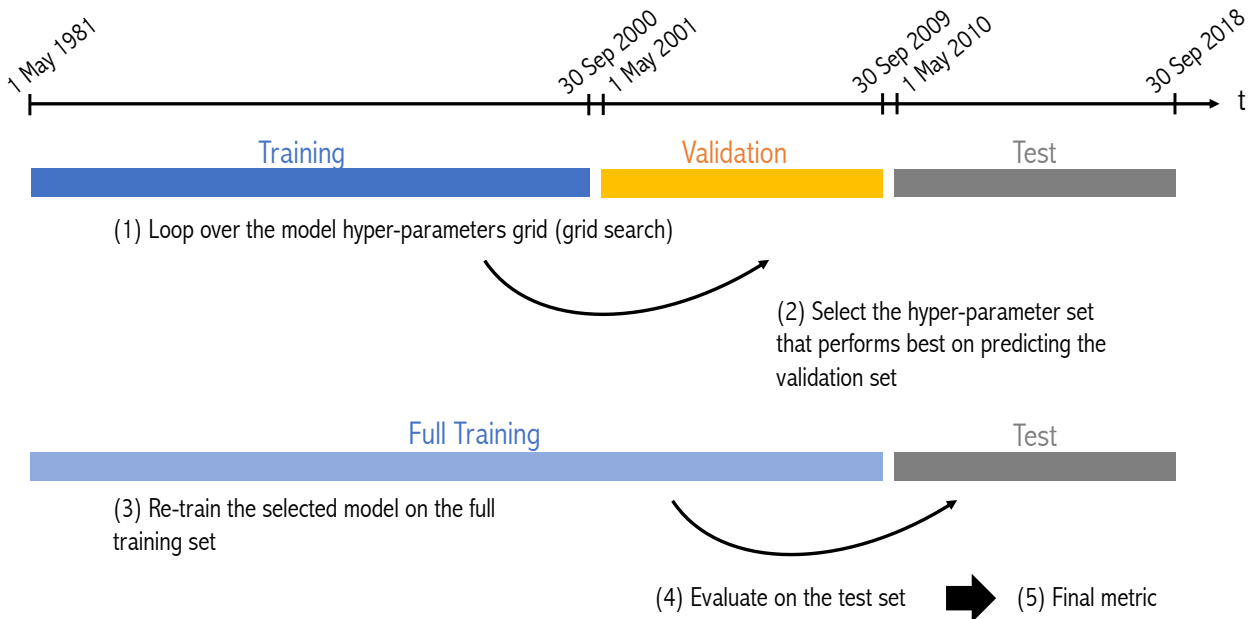


FIG. 3. Schematic of the training-validation-test split

246 We split the available data into a training period (1 May 1981 – 30 September 2000), a validation
 247 period (1 May 2001 – 30 September 2009), and a testing period (1 May 2010 – 30 September 2018)
 248 (Fig. 3). The validation period is used to optimize the statistical model’s hyper-parameters for
 249 each lead time. After the hyper-parameter optimization, the model is re-trained on the full training
 250 period (1 May 1981 – 30 September 2009), which is the combination of the validation and the
 251 training period. A nested cross-validation (CV) scheme is also implemented (Appendix, Fig. B1).

252 For the RFs, we use an exhaustive grid-search hyper-parameter optimization including all
 253 possible combinations (750) of the following parameters: number of trees in the forest
 254 $\in \{50, 100, 200, 400, 600\}$, maximum tree depth $\in 5\text{--}14$, and a range of 15 values centered around
 255 the full training set’s length T_{ft} divided by 100 in steps of $T_{\text{ft}}/500$ for the minimum number of
 256 samples per leaf. The minimum number of samples for splitting a node is set to the minimum
 257 number of samples per leaf multiplied by a factor of two and, for classification, the class weight
 258 is set to *balanced*. For the two linear models, the complexity parameter α is selected from the
 259 range $[0, 1]$ in steps of 0.05. The reference metrics for optimization are the root mean-square
 260 error (RMSE) for regression and the Brier score (BS) for classification (Section 2e). The selected
 261 hyper-parameters are shown in the Appendix (Table C1).

262 *e. Metrics for the evaluation of forecasting performance*

263 1) REGRESSION METRICS

264 For regression, two different metrics are considered: RMSE and Pearson correlation. The RMSE
 265 evaluates how far away the forecast ($\hat{\mathbf{y}}$) and the ground truth (\mathbf{y}) time series are from each other
 266 and is defined as:

$$\text{RMSE}(\hat{\mathbf{y}}, \mathbf{y}) = \sqrt{\text{MSE}(\hat{\mathbf{y}}, \mathbf{y})} = \sqrt{\frac{1}{T} \sum_{t=1}^T (\hat{y}_t - y_t)^2} \quad (2)$$

267 for T the number of time steps (sample size).

268 The Pearson correlation measures to what extent the curve follows the changes and is given by:

$$\text{Corr}(\hat{\mathbf{y}}, \mathbf{y}) = \frac{\sum_{t=1}^T (\hat{y}_t - \bar{\hat{\mathbf{y}}})(y_t - \bar{\mathbf{y}})}{\sqrt{\sum_{t=1}^T (\hat{y}_t - \bar{\hat{\mathbf{y}}})^2} \sqrt{\sum_{t=1}^T (y_t - \bar{\mathbf{y}})^2}} \quad (3)$$

269 for $\bar{z} = \frac{1}{T} \sum_{t=1}^T z_t$ the mean over all time steps.

270 2) CLASSIFICATION METRICS

271 For classification, the BS and the Receiver Operating Characteristic (ROC) Area Under Curve
 272 (AUC) are used to evaluate the probabilistic forecast. The BS is the mean squared error of the
 273 probability forecasts (i.e., Eq. 2 squared), considering that an observation is $y_t = 1$ if the event
 274 occurs and $y_t = 0$ if the event does not occur at time t . Since individual probabilistic forecasts and
 275 observations are bounded by zero and one, the BS can only take values in the range [0,1] (Wilks
 276 2019, chap. 9).

277 The ROC is the true positive rate (TPR) as a function of the false positive rate (FPR) (Bradley
 278 1997). The TPR (or Recall) is defined as the proportion of positive data points that are correctly
 279 considered positive, with respect to all positive data points. The TPR is given by $TP / (FN+TP)$
 280 for true positives (TPs) and false negatives (FNs). The FPR (or False Alarm) is defined as the
 281 proportion of negative data points that are mistakenly considered positive, with respect to all
 282 negative data points. The FPR is calculated as $FP / (FP+TN)$ for false positives (FPs) and true
 283 negatives (TNs) (see Table 4 for the definition of TP, FP, FN, and TN).

		Actual value (y)	
		Positive (1)	Negative (0)
Forecast value (\hat{y})	Positive (1)	TP	FP
	Negative (0)	FN	TN

284 TABLE 4. **Confusion matrix.** The positive class corresponds to a heatwave and the negative class to no
 285 heatwave. For a sensible model, the principal diagonal values must be high and the off-diagonal values must be
 286 low (Bradley 1997).

287 Moreover, the performance of the binary classification is assessed via the FPR-to-TPR ratio,
 288 extremal dependence index (EDI), and frequency bias (B). The EDI is used to evaluate forecasts
 289 of rare binary events and is calculated as (Ferro and Stephenson 2011):

$$EDI = \frac{\ln(FPR) - \ln(TPR)}{\ln(FPR) + \ln(TPR)} \quad (4)$$

290 This score is ill-defined if any of the four cells in the confusion matrix (Table 4) equals zero,
291 since $\ln(0)$ or a division by zero yield infinity. However, such models can still be interpreted by
292 adding an infinitely small number (pseudo-count) to those cells containing zeros (Wunderlich et al.
293 2019).

294 The frequency bias is the ratio of the number of positive-class forecasts to the number of
295 positive-class observations:

$$B = \frac{TP + FP}{TP + FN} \quad (5)$$

296 Unbiased forecasts exhibit $B = 1$, indicating that the event is forecast the same number of times
297 as observed (Wilks 2019, chap. 9).

298 We define a *useful* probabilistic forecast as having $BS < 0.25$ (Steyerberg et al. 2010) and ROC
299 $AUC > 0.5$ (Bradley 1997). We consider a binary forecast *useful* if $FPR/TPR < 1$ and $EDI > 0$
300 (Wilks 2019, chap. 9). In addition, B should be as close to one as possible.

301 *f. Calibration of the classification forecasts*

302 Good forecasts should not only be accurate (as measured by ROC AUC, EDI and the FPR-to-TPR
303 ratio) but also well-calibrated (as measured by BS and B) (Jolliffe and Stephenson 2005), meaning
304 that the sub-sample relative frequency should be exactly equal to the forecast probability in each
305 sub-sample (Wilks 2019, chap. 9). For example, if a model forecasts 100 positive-class events
306 (e.g., heatwave weeks), each with a probability of 80%, we expect 80 of the events to be correctly
307 classified (i.e., to actually be a heatwave).

308 1) PLATT SCALING FOR THE PROBABILISTIC FORECASTS

309 Unlike accuracy, reliability can be improved in a post-processing step by calibrating the proba-
310 bilistic forecasts (Jolliffe and Stephenson 2005). The linear ML models already predict calibrated
311 probabilities and do not need an additional calibration step. We use Platt scaling to re-calibrate the
312 probabilistic forecasts by the RFs. Platt scaling consists in projecting the (ill-calibrated) probab-
313 ilities predicted by the ML models onto the right probability distribution using a logistic regression
314 model (Smola et al. 2000, chap. 5). The RFs are trained on the training set and calibrated on the
315 validation set to determine the parameters of the logistic regression. The calibrated RF models are

316 then used to predict the test set. These datasets correspond to the ones defined in Fig. 3. Since the
317 logistic function is monotonic, the calibration via Platt scaling does not change the ordering of the
318 samples, and, consequently, the ROC AUC score remains the same. Instead, the BS is considerably
319 reduced after the calibration step.

320 2) PROBABILITY THRESHOLD MOVING FOR THE BINARY FORECASTS

321 Forecasting the two weekly summer heatwave indices defined in Section 2a3 ($+1\sigma$ and $+1.5\sigma$)
322 results in imbalanced classification problems (Table 3). A binary classifier trained on these
323 imbalanced data will learn to always forecast the negative class, leading to a trivial and ill-calibrated
324 statistical model. Balancing the data before the training or moving the probability threshold are
325 two potential solutions to this problem. Random undersampling and oversampling methods have
326 been explored to balance the training data (Lemaitre et al. 2017). However, these methods are
327 not used for the final version of the statistical models since, in this particular case, they result in
328 over-forecasting heatwaves.

329 Instead, for this study, the data imbalance is accounted for by adjusting the probability threshold:
330 The (non-calibrated) classification models output a probability for each validation sample to belong
331 to the positive class. Then, the probability threshold between zero and one that corresponds to no
332 frequency bias (i.e., $B = 1$) on the validation set is selected to binarize the output (Wilks 2019,
333 chap. 9). To avoid a strong dependency on the distribution of the validation set, an internal
334 cross-validation scheme is used for selecting the probability threshold. Thirty validation sets of
335 nine randomly selected non-consecutive years belonging to the full training set (1981–2009) are
336 constructed. The remaining 20 years are used for training. The threshold that minimises the
337 deviation from the mean frequency bias of the 30 validation sets from one is selected.

338 g. *Reference forecasts*

339 We compare our statistical models to the climatology, persistence, and ECMWF hindcast fore-
340 casts:

341 (i) *Climatology* For regression, temperature anomalies with respect to climatology are forecast.
342 Thus, the climatology forecast is zero for all times per definition. For classification, the climatology
343 forecast is the mode class for each day of the year. Since, in our dataset, the negative class

344 predominates strongly over the positive class, the climatology forecast is found to always predict
345 the negative class (no heatwave).

346 *(ii) Persistence* Persistence forecasts predict that the future weather condition will be the same
347 as the present condition. In practice, the persistence forecast is defined as keeping the value from
348 initialization time until verification time. For instance, for the regression forecast at two weeks
349 lead time, the persistence is the temperature anomaly two weeks before verification time.

350 *(iii) ECMWF* Early warnings are issued by the operational ECMWF sub-seasonal prediction
351 system, using 51 ensemble members and information beyond the ensemble mean. However, these
352 forecasts are currently only available for the years 2015–2022. Therefore, in order to evaluate
353 our ML models' skill for the full test period (2010–2018), we compare to ECMWF sub-seasonal
354 hindcast system's ensemble mean instead. This hindcast system is initialized twice a week and
355 provides 20-year hindcasts with 11 ensemble members integrated over 46 days. The hindcasts used
356 here cover the period 2000–2019 and use the model version of the Integrated Forecasting System
357 cycle 47r1 (Haiden et al. 2019).

358 The mean daily 2m-air temperature is downloaded at a spatial resolution of $1^\circ \times 1^\circ$ and the
359 arithmetic mean of the area over CE (as defined in Fig. 1) is calculated. Then, the temperature
360 anomalies are calculated by removing the lead-time-dependent climatology at each initialization,
361 calculated by the 20-year mean of the 11-member ensemble started on the same day and month
362 for each year of the reference period (2000–2019). For instance, if a hindcast was initialized on
363 May 31st, the lead time dependent climatology corresponding to that hindcast is calculated as the
364 mean of the 11-member ensemble initialized on May 31st and averaged over the 20-year reference
365 period (2000–2019) separately for each of the 46 days. After the calculation of the temperature
366 anomalies, a 7-day rolling mean is applied for each initialization. In this way, we end up with 40
367 days per initialization, with each day being the centre of the 7-day rolling mean. For instance, the
368 first day predicted by the initialization on May 31st will be June 4th (average over June 1st–June
369 7th).

370 Removing different climatologies for individual dynamical models and reanalysis or observational
371 datasets is standard practice, as the climatological normals are slightly different across datasets
372 (IPCC 2013, chap. 9). Moreover, in the case of sub-seasonal forecasting, calculating anomalies
373 with respect to a lead-time dependent climatology is expected to remove systematic biases which are

374 lead-time dependent (Manzanas 2020; Molteni et al. 2011). However, the methodology followed for
 375 the calculation of the dynamical model’s climatology can influence the forecast’s skill (Manrique-
 376 Suñén et al. 2020).

377 *h. Ensembles and uncertainty estimation*

378 For both ECMWF and the ML models, the final forecast is calculated as the mean forecast by an
 379 ensemble of K models:

$$\mu(\hat{\mathbf{Y}}) = \frac{1}{K} \sum_{k=1}^K \hat{\mathbf{y}}_k \quad (6)$$

380 with $\hat{\mathbf{y}}_k$ the time series prediction by each ensemble member. Then, the M metrics ψ_m defined
 381 in Section 2e for the final forecast are calculated as $\psi_m(\mu(\hat{\mathbf{Y}}), \mathbf{y})$, for $m = 1, \dots, M$. To quantify
 382 the uncertainty of these metrics, the M metrics are calculated with respect to the ground truth (\mathbf{y})
 383 for each ensemble member ($\psi_{m,k} = \psi_m(\hat{\mathbf{y}}_k, \mathbf{y})$). Then, for each metric m , the unbiased standard
 384 deviation of the ensemble ($\sigma_m(\hat{\mathbf{Y}})$) is used to represent the uncertainty of the final forecast’s
 385 metrics:

$$\sigma_m(\hat{\mathbf{Y}}) = \sqrt{\frac{1}{K-1} \sum_{k=1}^K (\psi_{m,k} - \mu(\psi_m))^2} \quad (7)$$

386 for $\mu(\psi_m) = \frac{1}{K} \sum_{k=1}^K \psi_{m,k}$ the mean metric m of all models in the ensemble.

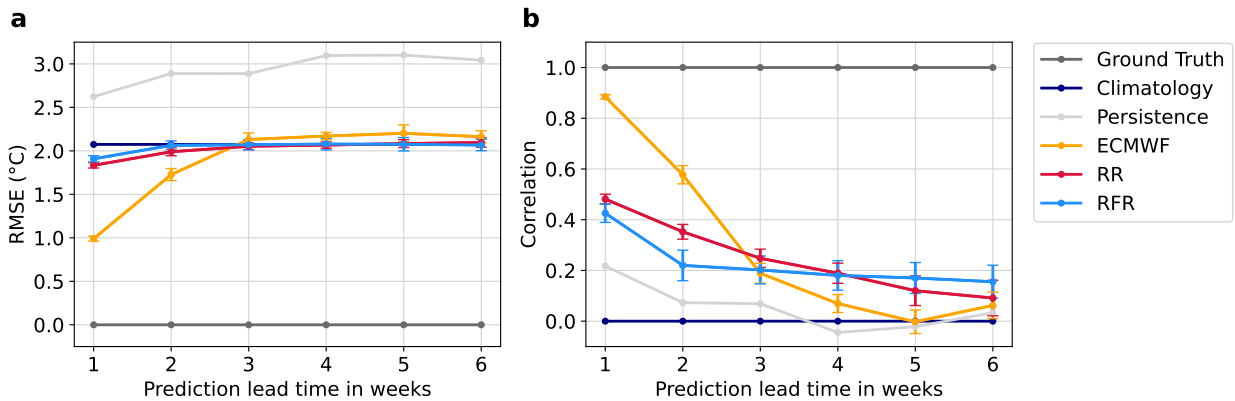
387 For ECMWF, the considered ensemble consists of $K = 11$ sub-seasonal hindcasts. For both the
 388 linear and RF models, block bootstrapping is used to create an ensemble. Bootstrapping consists
 389 of randomly drawing samples with replacement from the full training dataset (as defined in Section
 390 2d), with each sample having the same size as the original training dataset. Bootstrap resampling
 391 generally results in $\approx 37\%$ of the observations not being selected. This resampling procedure is
 392 repeated $K = 600$ times, producing K bootstrap training datasets used to train K ML models (Hastie
 393 et al. 2009, chap. 7). However, standard bootstrapping fails to represent the statistics of dependent
 394 data, like time series. Block bootstrapping overcomes this limitation by resampling independent
 395 chunks of continuous observations instead of single dependent ones (Kunsch 1989). Therefore,
 396 under the assumption of inter-annual independency of summers, we apply block bootstrapping

397 with a block size of one year, which means that the smallest unit considered for resampling is one
398 year instead of one day.

399 3. Results and discussion

400 a. Forecasts

401 1) REGRESSION FORECASTS



402 FIG. 4. **Performance of the regression models for six different lead times.** (a) RMSE and (b) correlation
403 for the regression forecasts. An accurate forecast is characterized by a low RMSE and a high correlation. The
404 error bars show the uncertainty of each forecast estimated via the standard deviation of the ensemble.

405 In Figure 4, the regression forecasts by two different ML models (RR and RFR) at six different
406 lead times (1–6 weeks) are compared to three reference forecasts: climatology, persistence, and
407 ECMWF. The analogous results for nested CV are shown in the Appendix (Fig. B2).

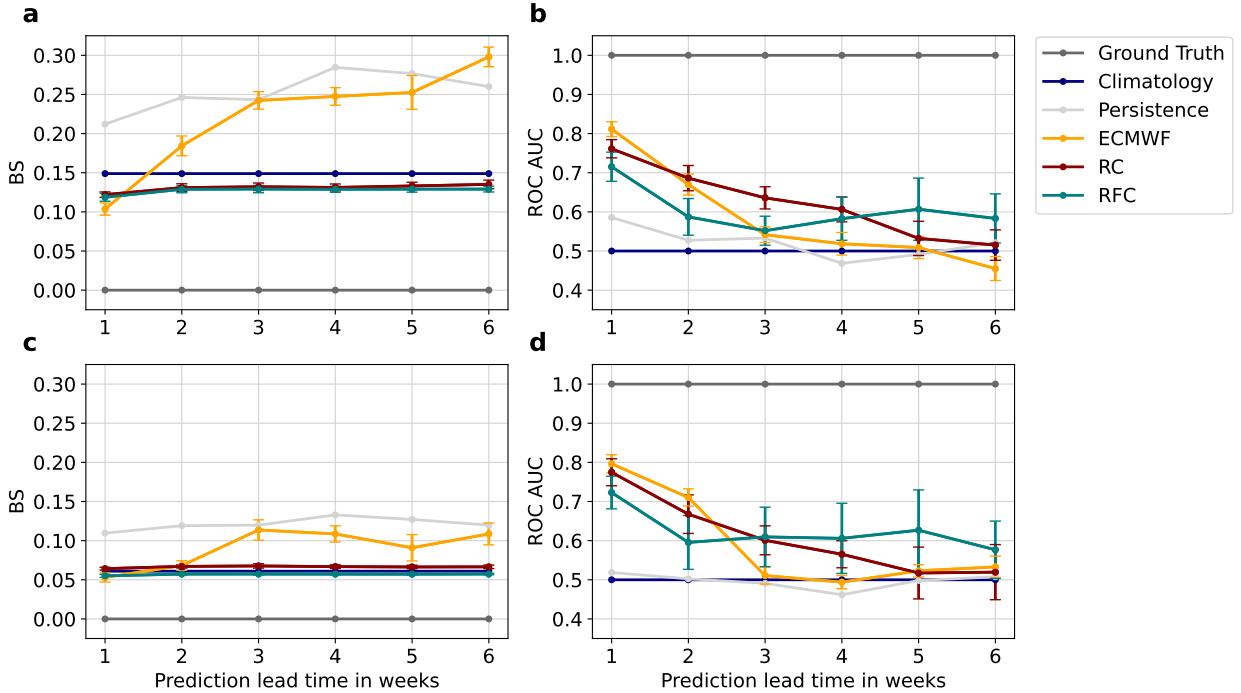
408 As can be observed in Fig. 4, all metrics are best for a lead time of one week. The uncertainty
409 in the forecasts by most models, which is represented by the error bars, increases with lead time.
410 The RR’s performance decays linearly with increasing lead time, with a correlation that ranges
411 from 0.48 for one week lead time to 0.09 for six weeks lead time. The RF’s correlation decreases
412 overall from one to six weeks lead time (from 0.43 to 0.16) but remains noticeably constant for
413 lead times longer than two weeks. The evolution of the RMSE is similar, but with the difference
414 that it saturates when reaching the RMSE value that corresponds to the climatology forecast. The
415 RMSE for the best statistical model at each lead time ranges between 1.83 for one week lead time
416 and 2.07 at six weeks lead time.

417 The linear ML model outperforms the RF in terms of correlation at short lead times (up to three
418 weeks), but the RF model provides a better forecast at long lead times (5–6 weeks). Both ML
419 models outperform the persistence forecast at all lead times. However, the climatology forecast
420 has a relatively low RMSE, being a comparatively good guess at long lead times, when forecasting
421 becomes difficult. For lead times longer than two weeks, the RMSEs of the ML models saturate at
422 the climatology’s RMSE and the ensemble mean of ECMWF’s hindcast has a worse RMSE than
423 the climatology forecast. Still, the climatology forecast does not correlate with the ground truth
424 and the ML and ECMWF models outperform climatology at all lead times in terms of correlation,
425 since these models always correlate positively with the ground truth. While ECMWF provides
426 highly skilled forecasts in terms of correlation and RMSE for one and two weeks lead time, the
427 skill decreases fast with increasing lead time; for lead times of three weeks and longer, the ML
428 models forecast the temperature anomalies more accurately than the ensemble mean of ECMWF’s
429 hindcast.

430 The ML models generally pick up the sign of the anomalies but their sharpness, which refers to
431 the ability of a probabilistic forecast to spread away from the climatological average (Gneiting et al.
432 2007), is lower than the one from ECMWF and extreme values are not well-captured (Appendix,
433 Fig. A1). For longer lead times, all models exhibit low sharpness in their forecasts, tending to
434 the climatology forecast. In the case of the ML models, this tendency towards climatology can
435 be a consequence of the loss function. The loss functions for the RR and the RFR models are
436 the linear least squares function and the mean squared error, respectively. Both metrics measure
437 the distance between the forecast and the target curves. Since forecasting anomalies accurately
438 becomes more difficult with increasing lead time, a statistical model that is trained to minimise the
439 error will tend to forecast the mean of the distribution of possible outcomes, becoming smoother
440 and losing sharpness compared to the observations (Rasp and Thuerey 2021). ML models trained
441 to optimize alternative loss functions, like in the study by Lopez-Gomez et al. (2022), would be
442 worth exploring.

443 2) CLASSIFICATION FORECASTS

449 The classification models output a probability for each sample in the test set to belong to the
450 positive class (i.e., for a week to be classified as a heatwave week). These probabilities are calibrated



444 **FIG. 5. Performance of the probabilistic classification models for six different lead times.** BS and ROC
 445 AUC for the $+1\sigma$ (a&b) and $+1.5\sigma$ (c&d) weekly heatwave indices. An accurate probabilistic classification
 446 forecast is characterized by a low BS and a high ROC AUC. A no-skill probabilistic classification forecast is
 447 represented by a BS of 1 and a ROC AUC of 0.5 (as indicated by the climatology). The error bars show the
 448 uncertainty of each forecast estimated via the standard deviation of the ensemble.

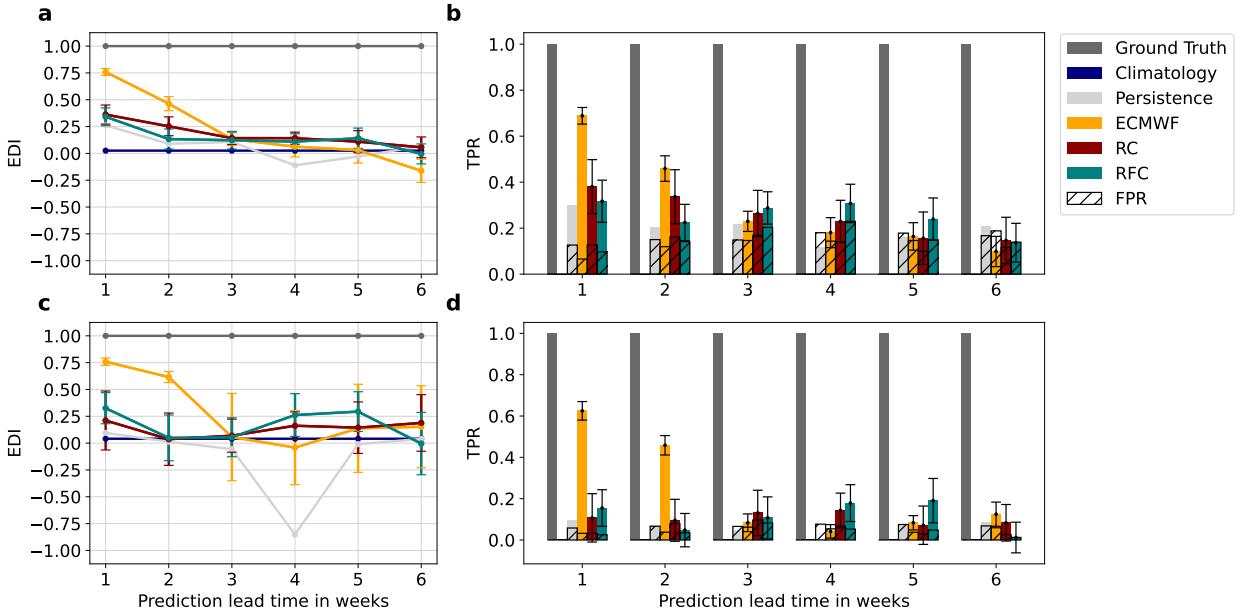
451 to obtain the probabilistic forecast for the RFC model and kept unchanged for the RC model. For
 452 both classifiers, the non-calibrated probabilities are binarized via a probability threshold, meaning
 453 that a zero (no heatwave) or a one (heatwave) is assigned to each sample in the test set (Section
 454 2f). In Figure 5, the probabilistic classification forecasts by two ML models (RC and RFC) at six
 455 different lead times (1–6 weeks) are compared to the three reference forecasts. In Figure 6, the
 456 performance of the binary classification is shown. The analogous results for nested CV are shown
 457 in the Appendix (Figs. B3 and B4). Two different heatwave indices are used: $+1\sigma$ for high and
 458 $+1.5\sigma$ for extremely high temperature anomalies (Section 2a3).

459 For the probabilistic forecasts, the linear models have a higher ROC AUC than the RFCs for
 460 short lead times (up to four weeks for the $+1\sigma$ heatwave index and up to two weeks for the $+1.5\sigma$
 461 heatwave index). However, the RFCs' ROC AUC remains more constant than the linear models'

462 ROC AUC across lead times, outperforming the linear models for longer lead times (Figs. 5b&d).
463 Moreover, the probabilistic forecasts by both classification ML models outperform persistence and
464 climatology at all lead times and the ensemble mean of ECMWF's hindcast for lead times longer
465 than two weeks, except for the $+1.5\sigma$ forecast at lead times of 5–6 weeks by the RC model. Overall,
466 the forecast uncertainties by all models increase with lead time, resulting in overlapping error bars.
467 These patterns are analogous to the ones observed for the regression forecast (Fig. 4b). In terms of
468 BS, both statistical models present a smaller loss than the ensemble mean of ECMWF's hindcast
469 at lead times of two weeks and higher (Figs. 5a&c). As for regression, the climatology shows a
470 constant Brier loss, which is comparable to the BS of the ML models. The probabilistic forecasts
471 by both statistical models (taking the uncertainty into account) are *useful* at each of the considered
472 lead times (1–6 weeks), except for the RC model at 5–6 weeks lead time, where the uncertainty
473 bars overlap with the no-skill ROC AUC score. Meant by *useful* is $BS < 0.25$ and $ROC\ AUC > 0.5$.
474 It is remarkable that non-null skill by the RFC model is present at these long lead times.

475 Moreover, in terms of Brier loss, extremely high temperature anomalies ($+1.5\sigma$) are easier to
476 forecast than high temperature anomalies ($+1\sigma$), which agrees with the findings of Wulff and
477 Domeisen (2019). The performance of the ensemble mean of ECMWF's hindcast in predicting
478 extremely high temperature anomalies ($+1.5\sigma$) drops drastically between two and three weeks
479 lead time and remains constant for lead times longer than three weeks. In contrast, ECMWF's
480 classification skill when forecasting high temperature anomalies ($+1\sigma$) decays close to linearly
481 with lead time. The probabilistic RFC is slightly more skilled in capturing extremes than the
482 probabilistic linear model: the RFC forecasts extremely high temperature anomalies ($+1.5\sigma$) more
483 accurately than high temperature anomalies ($+1\sigma$) compared to the linear model. This difference
484 in skill is possibly due to non-linear effects driving extreme temperature which the RFC is able to
485 capture but the linear model is not.

487 For the binary classification, the overall skill of the statistical models is poorer than for the
488 probabilistic classification. As the lead time increases, the two statistical models and the ensemble
489 mean of ECMWF's hindcast predict fewer weekly heatwave events and the TPR decreases with
490 lead time (Figs. 6b&d). Moreover, despite moving the probability threshold to forecast an unbiased
491 validation set (Section 2f2), the binary forecasts of the test set by the statistical models (in particular,
492 for the $+1.5\sigma$ heatwave index) are considerably biased compared to the predictions by the ensemble



486 **FIG. 6. Performance of the binary classification models for six different lead times.** (a) EDI and (b) TPR
 487 (coloured bars) and FPR (stippled bars) for the $+1\sigma$ weekly heatwave index. (c) and (d) are the corresponding
 488 forecasts for the $+1.5\sigma$ weekly heatwave index. An accurate binary classification forecast is characterized by
 489 a high EDI, a high TPR, and a low FPR. The error bars show the uncertainty of each forecast estimated via the
 490 standard deviation of the ensemble. Since the climatology forecast predicts only zeros (no heatwave), both its
 491 TPR and FPR are equal to zero at all lead times (Figs. b&d). Moreover, at a lead time of four weeks, there is
 492 no overlapping between the $+1.5\sigma$ heatwave events in the ground truth and persistence forecast, resulting in zero
 493 hits ($TP = 0$). Therefore, the EDI is not defined for the persistence forecast at this lead time and the pseudo-count
 494 correction yields a considerably lower value for the EDI compared to the persistence forecast at the other lead
 495 times (Fig. c). This is an artifact of the limited sample size and does not appear in nested CV (Appendix, Fig.
 496 B4c).

503 mean of ECMWF's hindcast (Table 5). *Useful* binary forecasts by at least one of the statistical
 504 models (taking the uncertainty into account) are found at 1–5 weeks lead time for the $+1\sigma$ heatwave
 505 index and at lead times of one, four, and five weeks for the $+1.5\sigma$ heatwave index, where *useful* is
 506 defined as $FPR/TPR < 1$ and $EDI > 0$.

511 Finally, the RFC tends to overfit the training set considerably, with ROC AUCs and EDIs above
 512 0.99 at all considered lead times (1–6 weeks). The hyper-parameters chosen during the grid search

Heatwave index	Model	1 week	2 weeks	3 weeks	4 weeks	5 weeks	6 weeks
$+1\sigma$	RC	1.11 ± 0.37	1.26 ± 0.47	1.23 ± 0.49	1.03 ± 0.46	0.72 ± 0.58	0.81 ± 0.57
	RFC	0.87 ± 0.29	1.03 ± 0.31	1.45 ± 0.36	1.62 ± 0.44	1.09 ± 0.46	0.93 ± 0.43
	ECMWF	1.05 ± 0.04	1.11 ± 0.10	1.03 ± 0.11	0.97 ± 0.14	0.97 ± 0.18	1.13 ± 0.12
$+1.5\sigma$	RC	0.61 ± 0.71	1.32 ± 0.95	1.62 ± 1.23	1.18 ± 1.07	0.52 ± 1.13	0.49 ± 0.92
	RFC	0.55 ± 0.42	0.58 ± 0.58	1.38 ± 0.81	0.99 ± 0.59	0.93 ± 0.75	0.20 ± 0.63
	ECMWF	1.12 ± 0.08	1.04 ± 0.14	1.04 ± 0.22	0.88 ± 0.18	0.67 ± 0.31	1.04 ± 0.27

507 TABLE 5. **Frequency bias** of the ensemble mean forecasts of each of the two classification targets in the test
508 period (2010–2018) by the two ML models (RC and RFC) and ECMWF’s hindcast. A well-calibrated model
509 should have $B = 1$. For $B < 1$, the forecast underestimates the total number of heatwave events and for $B > 1$, the
510 events are overestimated. Biases of the ensemble mean forecasts above 1.5 or below 0.5 are bold.

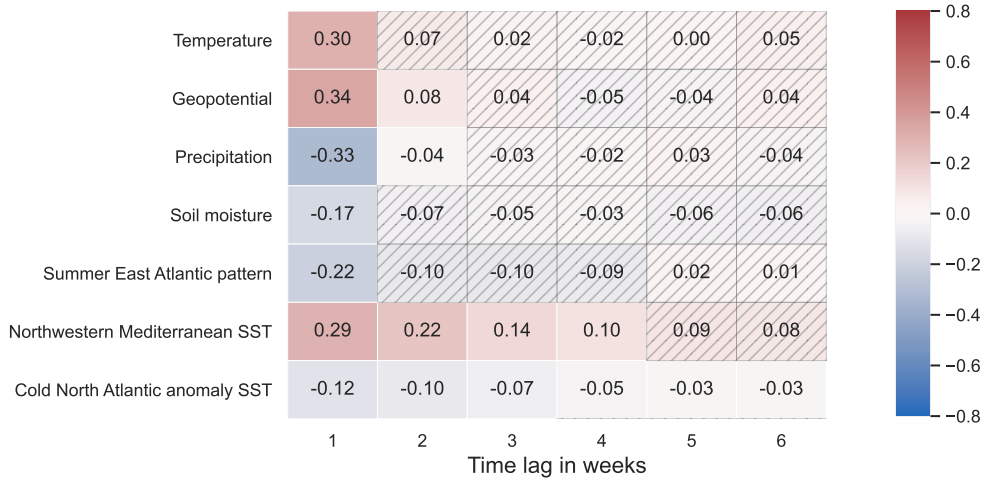
513 for the RFC correspond to the deepest possible trees and the smallest possible leaves (Appendix,
514 Table C1).

515 *b. Predictor importance*

516 The relevance of each of the seven predictors for forecasting summer temperature anomalies
517 is investigated by performing a linear correlation analysis and examining which predictors were
518 predominantly used by each ML model.

519 1) LINEAR CORRELATION ANALYSIS

523 In Figure 7, the linear correlations between the *temperature* and the predictors in the extended
524 summer season (MJJAS) are shown for six different time lags (1–6 weeks). At short time lags,
525 the *temperature* shows a strong autocorrelation. The *geopotential* has an even stronger positive
526 correlation to the *temperature*, indicating that during anticyclonic conditions higher temperatures
527 than normal are expected. In contrast, *precipitation*, *soil moisture*, and the *SEA* index correlate
528 negatively with *temperature* at short time lags. *Precipitation* is associated with cyclones, cloudy
529 conditions, and lower surface air temperatures. Moreover, dryness (low *soil moisture*) and high
530 *temperature* reinforce each other (Section 1). The correlations with the atmospheric predictors
531 (*temperature*, *geopotential*, *precipitation*, and *SEA*) decay fast. In addition, the linear correlation
532 with *soil moisture* becomes non-significant for lead times of two weeks and longer. In contrast,
533 the SST predictors show a more constant linear correlation over time and dominate on timescales



520 FIG. 7. **Lagged linear correlations between the predictors and the *temperature*** in the extended summer
 521 season (MJJAS) at weekly time resolution. Hatched cells correspond to non-significant linear Pearson correlation
 522 coefficients at 5% significance level.

534 longer than a week, since they are more persistent. While the *NWMED SST* correlates positively
 535 with the *temperature* over CE, the *CNAA SST* correlates negatively with both.

536 2) RELEVANCE OF LAGGED PREDICTORS FOR THE MACHINE LEARNING MODELS

537 Each of the seven predictors is provided to the ML models at four time lags, building a set of 28
 538 lagged predictors for each lead time (Section 2a2). The relevance of a lagged predictor for each
 539 ML model is given by the absolute value of its correlation coefficient for the linear models and its
 540 feature importance for the RF models. Here, the impurity-based feature (or Gini) importance for
 541 a predictor X_i is computed by the sum of all impurity decrease measures of all nodes in the forest
 542 at which a split based on X_i has been conducted, normalized by the number of trees (Menze et al.
 543 2009; Nembrini et al. 2018). These values are shown in Tables D1 and D2 for the linear models
 544 (RR and RC, respectively) and in Tables D3 and D4 for the RFs (RFR and RFC, respectively) in
 545 the Appendix.

546 In general, predictors at short lags are more useful to the statistical models. Also, the longer
 547 the forecast's lead time, the higher the relative contribution from SST becomes. The location of
 548 the most important SST region is lead-time dependent: the *NWMED SST* dominates for short lead
 549 times (up to two weeks) and the *CNAA SST* prevails for longer lead times (3–6 weeks). The *CNAA*

550 SST's dominance at long lead times is consistent with the linear correlation shown in Fig. 7, which
551 remains significant for CNAA SSTs at the longest lead times.

552 When forecasting the $+1\sigma$ and the $+1.5\sigma$ heatwave indices, the overall set of relevant lagged
553 predictors is similar, with two exceptions: First, the SST is used more to forecast high temperature
554 anomalies ($+1\sigma$) compared to extremely high temperature anomalies ($+1.5\sigma$). Second, the RFC
555 model relies more on *soil moisture* to forecast extremely high temperature anomalies ($+1.5\sigma$)
556 compared to high temperature anomalies ($+1\sigma$), coinciding with the findings by Lopez-Gomez
557 et al. (2022). The different importances of the SST and *soil moisture* for forecasting the two
558 heatwave indices could be due to the positive feedback between temperature and soil moisture
559 (Section 1) being more pronounced for extremely high compared to high temperature anomalies.
560 Nevertheless, we can find more marked differences between the two families of statistical models:

561 (i) *Linear models* For the linear models, SSTs dominate at all lead times. In particular, the CNAA
562 SST is the most relevant predictor for the RR model at lead times of 2–6 weeks. Nonetheless,
563 the *temperature* is a useful predictor for the RR model at short lead times (1–3 weeks) as well.
564 At a lead time of one week, also the *precipitation* and *soil moisture* contribute to the regression
565 forecast. In contrast, these three lagged predictors are not used by the RC model, which relies
566 almost exclusively on SSTs. Therefore, the prediction skill of the ML models incorporating only
567 the NWMED and CNAA SST predictors has been tested additionally (Appendix, Figs. E1–E3).
568 The regression models have poorer prediction skill when using SST-based predictors only. The
569 RC probabilistic classification model benefits from including SST-only predictors at lead times
570 of 4–6 weeks for $+1.5\sigma$, indicating that the SSTs are the most important predictors for these
571 forecasts (Appendix, Table D2) and the other predictors only increase the model's complexity.
572 Overall, poorer prediction skill is observed for the binary classification models that use only SST
573 predictors, especially for the $+1.5\sigma$ prediction.

574 (ii) *RF models* For the RF models, *temperature*, *geopotential*, *precipitation*, the SEA index, and
575 NWMED SST at short lags are the most important predictors at short lead times (one week) and
576 SSTs are found to dominate for longer lead times (2–6 weeks). In addition, *soil moisture* and
577 the SEA index are useful at lead times of 3–6 and 1–5 weeks, respectively. At lead times longer
578 than one week, these two predictors have no significant linear correlation with the *temperature*
579 (Fig. 7) and are used by the RF models but not by the linear models. A plausible explanation

580 for this phenomenon is the presence of highly non-linear links between *temperature* and *soil*
581 *moisture*, and *temperature* and the *SEA* index. The physical mechanism behind the non-linear
582 link between *temperature* and *soil moisture* can be the positive feedback described in Section 1 as
583 well as threshold behavior. For example, over transitional wet/dry regimes, soil moisture exhibits
584 large variability and therefore air temperature can be altered by up to 6–7K, while typical soil
585 moisture variations can impact air temperature by up to 1.1–1.3K (Schwingshackl et al. 2017).
586 The SEA pattern and its relation to enhanced summer temperature anomalies resemble the one of
587 air temperature and the summer North Atlantic Oscillation (Folland et al. 2009). The anomalous
588 subsidence associated with the positive geopotential center of the SEA pattern over CE causes a
589 reduction of cloud cover and thus increased solar radiation and surface sensible heating. Increased
590 sensible heating can help maintain the anticyclone over land, contribute to further dryness of the
591 soil, and thus lead to a positive feedback loop with increasing temperatures. These two non-linear
592 links between *temperature* and *soil moisture*, and *temperature* and the *SEA* index (including *soil*
593 *moisture*) would explain the enhanced skill of the RF models compared to the linear models at lead
594 times higher than four weeks (Section 3a).

595 **4. Limitations and downstream tasks**

596 In this section, the current limitations are discussed and further research ideas to improve the
597 forecasts are suggested: (1) alternative statistical models, (2) approaches to overcome the limitations
598 due to the small sample size, and (3) non-operational statistical models.

599 (1) The statistical models used in our study belong to the field of classical ML. The complex nature
600 of climate data (e.g., non-linear dependencies between predictors, autocorrelation, and unobserved
601 predictors) poses important challenges to traditional ML models. As discussed in Section 1, DL
602 is also being used for extreme weather forecasting. DL can capture more complex relationships
603 between predictors and target, and might therefore be better suited to describe the mechanisms
604 behind heatwaves, which most likely include non-linear processes. In addition, classical ML
605 approaches benefit from domain-specific hand-crafted features to account for dependencies in
606 time or space but rarely exploit spatio-temporal dependencies exhaustively. In contrast, DL can
607 automatically extract abstract spatio-temporal features (Reichstein et al. 2019). Yet, DL models
608 require larger datasets than the ones used for this study and were therefore not used.

609 (2) One of the main limitations of this study is the size of the dataset. The initial dataset
610 is considerably larger, but precious information gets lost when taking the average over latitude-
611 longitude boxes. It might be interesting to explore the effect of using several smaller sub-boxes
612 instead of one large box. Additional columns could be added to the dataset, such as a box label or its
613 latitude-longitude coordinates. Also, the currently used boxes are rectangular and their coordinates
614 are chosen based on our physical understanding and the correlation to the target. This could be
615 refined by letting an algorithm select sub-regions of different shapes for each predictor based on
616 the correlation of each grid cell to the target (Vijverberg et al. 2020) or even including the spatial
617 information of the predictors (van Straaten et al. 2022). While lower-dimensional statistical models
618 like RR and RC might not be able to distinguish between distinct mechanisms acting in different
619 regions, RFs are expected to benefit from additional gridded observational data.

620 (3) The proposed ML models use input data at daily resolution and make weekly predictions.
621 Therefore, to provide the predictions by these models operationally, there is a need for input data
622 updates with at least weekly frequency. Since this high frequency of updates is not available for
623 the data from gridded observations used in this study, the proposed ML models cannot be used
624 operationally. ERA5 reanalysis data, which provides preliminary product updates every 5 days
625 (Hersbach et al. 2020), could be explored as an alternative input.

626 5. Conclusions

627 To conclude, we summarize the improvements on sub-seasonal central European temperature
628 anomalies and heatwave prediction by the chosen ML models: The performance of the linear and
629 RF models decays with lead time but outperforms persistence and climatology at all lead times.
630 ECMWF yields accurate forecasts for 1–2 weeks lead time but our ML models compete with the
631 ensemble mean of ECMWF’s hindcast at lead times longer than two weeks. While the linear
632 models perform better for shorter lead times (1–3 weeks), the RFs take over at lead times longer
633 than four weeks.

634 The statistical regression forecast of summer temperature is better than a random prediction in
635 forecasting the sign of the anomalies at all considered lead times (1–6 weeks) and outperforms
636 the ensemble mean of ECMWF’s hindcast at long lead times (3–6 weeks). However, extreme
637 values are poorly captured. For the classification problem, both statistical models yield a *useful*

638 probabilistic forecast (meaning $BS < 0.25$ and $ROC\ AUC > 0.5$) for each of the considered lead
639 times (1–6 weeks), except for the RC model at 5–6 weeks lead time. It is remarkable that non-null
640 skill by the RFC model is present at these long lead times. The binary forecast by at least one of
641 the statistical models is *useful* (meaning $FPR/TPR < 1$ and $EDI > 0$) at 1–5 weeks lead time for the
642 $+1\sigma$ heatwave index and at lead times of one, four, and five weeks for the $+1.5\sigma$ heatwave index
643 (Section 3a).

644 At short lead times (1 week), the following variables are found to be the best predictors of summer
645 temperature anomalies and heatwaves in CE: local 2-m air *temperature*, 500-hPa *geopotential*,
646 *precipitation*, and *NWMED SST*. At longer lead times (2–6 weeks), *NWMED* and *CNAA SST* are
647 the most relevant predictors. Moreover, the *SEA* index and *soil moisture* have a linear link with
648 *temperature* at one week lead time and a possible non-linear link at longer lead times (Section 3b).

649 In summary, even though our ML models cannot currently be used operationally, these statistical
650 models seem to capture a signal that the ensemble mean of ECMWF’s hindcast is not capturing.
651 ML models can, therefore, help extend the forecasting lead time of summer temperature anomalies
652 and heatwaves to sub-seasonal scales, and are a promising direction for further research in sub-
653 seasonal forecasting. Nevertheless, making better forecasts is not enough. Forecasts acquire value
654 through their ability to influence the decisions made by their users (Murphy 1993). As discussed
655 in the Introduction (Section 1), EWS involve not only forecasting the heatwave event but also
656 triggering effective and timely response plans that target vulnerable populations and regions. This
657 second step must also be successfully implemented to reduce the impact of such damaging events
658 (Merz et al. 2020; White et al. 2021).

659 *Acknowledgments.* This project has received funding from the European Research Council (ERC)
660 under the European Union’s Horizon 2020 research and innovation programme (project "HEAT-
661 forecast", Grant agreement No. 847456). Support from the Swiss National Science Foundation
662 through projects PP00P2_170523 and PP00P2_198896 to M. P. and D. D. is gratefully acknowl-
663 edged. J. C. is supported by the US National Science Foundation grants AGS-1657748, PLR-
664 1901352, and ARCSS-2115068. We thank O. Wulff for downloading a part of the data used for
665 this study. Also, we appreciate the recommendations from M. Murphy and A. Baldus Benet. We
666 acknowledge L. Grunwald for improving the English in the manuscript. Finally, we thank the three
667 anonymous reviewers for providing insightful comments which improved our work. The authors
668 declare no conflicts of interests.

669 *Data availability statement.* We have made the *Python* code used to perform the calculations
670 and generate the figures publicly available on GitHub.¹ The RR and RC functions belong to the
671 *linear model*, and the RFR and the RFC functions belong to the *ensemble* modules from *Sklearn*,
672 respectively (Pedregosa et al. 2011). The Pearson linear correlation test uses the TIGRAMITE
673 code by J. Runge, which is publicly available (Runge et al. 2019).² We acknowledge the E-OBS
674 dataset from the EU-FP6 project UERRA³ and the Copernicus Climate Change Service, and the
675 data providers in the ECA&D project (Cornes et al. 2018).⁴ The ERA-Interim (Dee et al. 2011)
676 and ERA5-Land (Muñoz-Sabater et al. 2021) data are provided by ECMWF.⁵ The HadISST data
677 (version 1.1) are provided by the Met Office Hadley Centre⁶ (Rayner et al. 2003). The ECMWF
678 S2S data are publicly accessible.⁷

¹www.github.com/bethweirich/hwai.git

²www.github.com/jakobrunge/tigramite

³www.uerra.eu

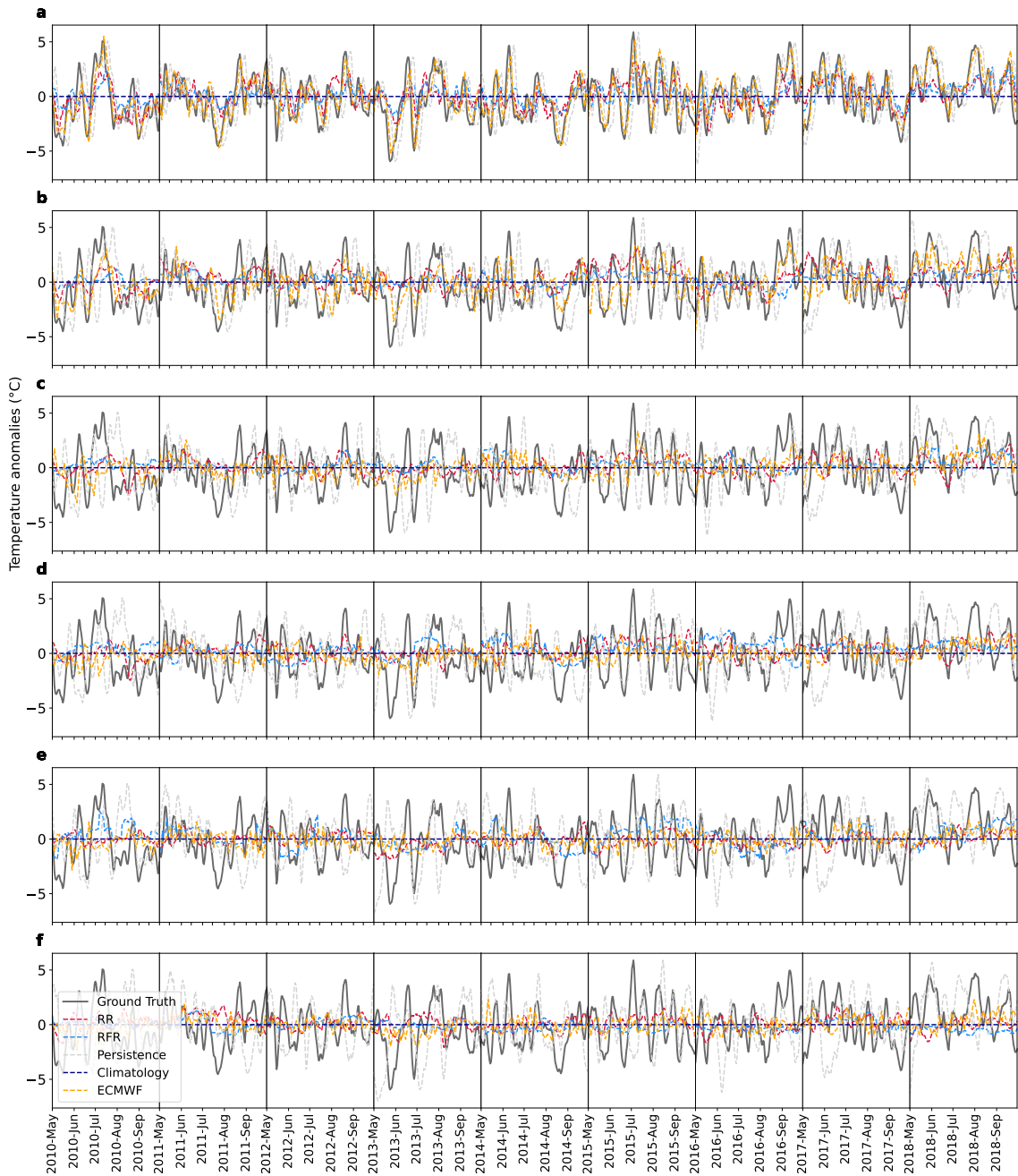
⁴www.ecad.eu

⁵www.ecmwf.int

⁶www.metoffice.gov.uk/hadobs

⁷apps.ecmwf.int/datasets/data/s2s

Regression forecasts' time series



681 **FIG. A1. Regression time series.** The ground truth time series, the reference forecasts, and the predictions by
682 the ML regression models of the temperature anomalies are shown for the nine summers in the test time period
683 (2010–2018). Figs. a–f correspond to lead times 1–6, respectively.

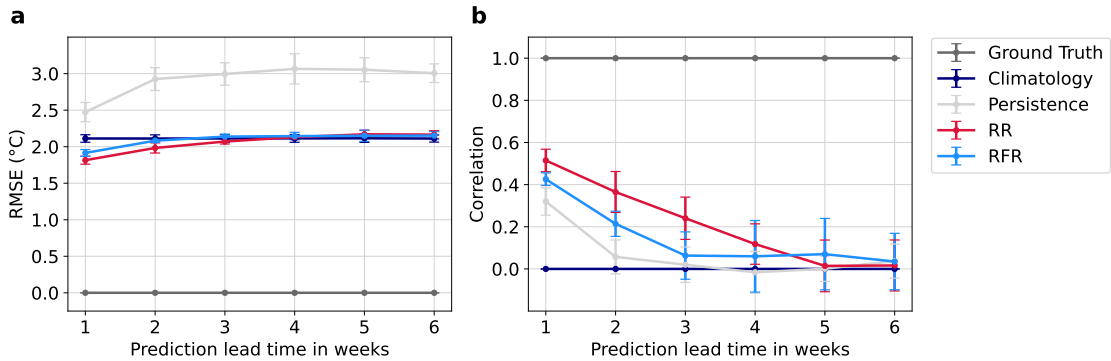
Nested Cross-Validation

To assess the robustness of our ML models, a CV scheme is implemented. In CV, the model is trained on different data subsets, which reduces overfitting and results in a better generalisation. Moreover, CV removes the dependency on an arbitrarily-selected test set (i.e., on decadal climate variability), making the metrics more robust (Vabalas et al. 2019). Here, a nested CV scheme with five outer and two inner splits is used (Fig. B1). The main benefit of nested CV compared to other CV schemes is that the statistical model is trained and tested on the full dataset while maintaining the independence of the test set, making this method well-suited for a limited sample size.

Nested CV is generally not used for time series data since consecutive time steps are strongly correlated. However, since the correlation between the considered predictors decays after a maximum of a few months and only summer data points are selected for this study, summers belonging to different years can be considered independent. To avoid a strong correlation between the sets at the splitting points, the data is split during the winter months.

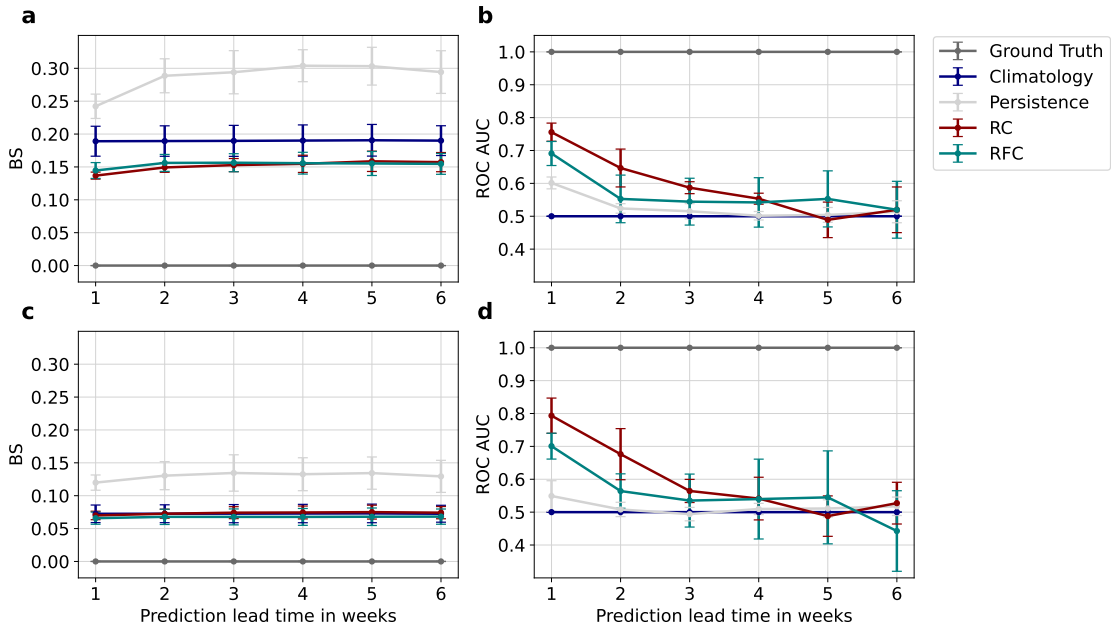


FIG. B1. **Nested cross-validation scheme.** $N = 5$ different test sets are predicted by the statistical models and the metrics with respect to the ground truth are calculated for each test set. The final metrics are obtained by averaging the metrics for the five test sets. The uncertainties of these metrics are estimated via the standard deviation of these 5-member ensembles. This figure is adopted from Vabalas et al. (2019).

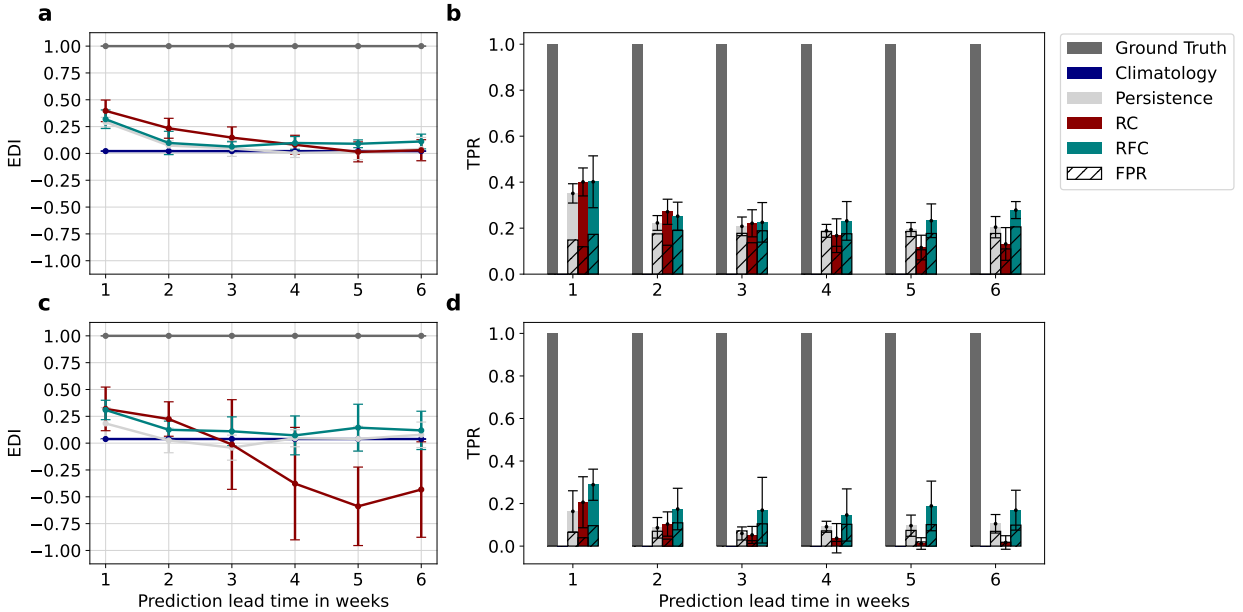


713 **FIG. B2. Performance of the regression models for six different lead times with nested CV.** (a) RMSE
 714 and (b) correlation for the regression forecasts. An accurate forecast is characterized by a low RMSE and a high
 715 correlation. The error bars show the uncertainty of each forecast estimated via the standard deviation of the
 716 ensemble.

702 The metrics obtained with nested CV (Figs. B2, B3, and B4) are similar, although smoother,
 703 compared to the results without CV (Figs. 4, 5, and 6), except for the binary classification by the
 704 RC model (Fig. B4c). The linear models also show higher skill than the RF models for lead times
 705 up to three weeks and the RFs outperform the linear models at 5–6 weeks lead time. While the
 706 skill of the ML models at short lead times (up to three weeks) is similar with and without CV,
 707 the models in nested CV perform slightly worse for longer lead times. Moreover, the uncertainty
 708 of the ML models is higher with nested CV. Therefore, while at least two ML models outperform
 709 persistence and climatology on average for all lead times, the error bars overlap with the reference
 710 forecasts for lead times of three weeks and longer. A comparison to the ECMWF forecast can not
 711 be included for nested CV, because the dynamical model is not available during the full test period
 712 used for this CV scheme (1981–2018).



717 **FIG. B3. Performance of the probabilistic classification models for six different lead times with nested**
 718 **CV.** BS and ROC AUC for the $+1\sigma$ (a&b) and $+1.5\sigma$ (c&d) weekly heatwave indices. An accurate probabilistic
 719 classification forecast is characterized by a low BS and a high ROC AUC. A no-skill probabilistic classification
 720 forecast is represented by a BS of 1 and a ROC AUC of 0.5 (as indicated by the climatology). The error bars
 721 show the uncertainty of each forecast estimated via the standard deviation of the ensemble.



722 **FIG. B4. Performance of the binary classification models for six different lead times with nested CV.** (a)
 723 EDI and (b) TPR (coloured bars) and FPR (stippled bars) for the $+1\sigma$ weekly heatwave index. (c) and (d) are
 724 the corresponding forecasts for the $+1.5\sigma$ weekly heatwave index. An accurate binary classification forecast is
 725 characterized by a high EDI, a high TPR, and a low FPR. The error bars show the uncertainty of each forecast
 726 estimated via the standard deviation of the ensemble. Since the climatology forecast predicts only zeros (no
 727 heatwave), both its TPR and FPR are equal to zero at all lead times (Figs. b&d).

Hyper-parameters

Target	Lead time (weeks)	α	Number of estimators	Min. samples/leaf	Max. depth
Temperature anomalies	1	1.0	100	20	5
	2	0.0	200	116	8
	3	1.0	100	52	5
	4	1.0	50	4	5
	5	1.0	200	12	5
	6	0.0	400	100	5
+1σ heatwave index	1	1.0	600	4	14
	2	0.95	400	4	14
	3	1.0	400	4	14
	4	0.0	600	4	14
	5	1.0	600	4	14
	6	1.0	600	4	14
+1.5σ heatwave index	1	1.0	600	4	14
	2	0.75	400	4	14
	3	1.0	600	4	14
	4	1.0	600	4	14
	5	1.0	600	4	14
	6	1.0	600	4	14

730 **TABLE C1. Optimized hyper-parameters.** Linear (α) and RF (number of estimators, minimum samples per
731 leaf, and maximum depth) hyper-parameters for three targets and six lead times.

APPENDIX D

Correlation coefficients and feature importances

Lead time		1 week	2 weeks	3 weeks	4 weeks	5 weeks	6 weeks
Predictor	Lag (weeks)						
Temperature	1	0.47	-	-	-	-	-
	2	-0.4	-0.3	-	-	-	-
	3	-0.23	-0.51	-0.42	-	-	-
	4	0.05	0.02	-0.07	-0.11	-	-
	5	-	0.26	0.35	0.31	0.26	-
	6	-	-	0.2	0.32	0.29	0.31
	7	-	-	-	-0.28	-0.22	-0.14
	8	-	-	-	-	-0.14	-0.08
	9	-	-	-	-	-	-0.07
Geopotential	1	0.07	-	-	-	-	-
	2	0.21	0.21	-	-	-	-
	3	0.14	0.33	0.25	-	-	-
	4	-0.22	-0.17	-0.14	-0.13	-	-
	5	-	-0.3	-0.38	-0.37	-0.4	-
	6	-	-	-0.18	-0.34	-0.31	-0.32
	7	-	-	-	0.29	0.15	0.08
	8	-	-	-	-	0.25	0.18
	9	-	-	-	-	-	0.15
Precipitation	1	-0.66	-	-	-	-	-
	2	0.07	0.22	-	-	-	-
	3	0.21	0.27	0.3	-	-	-
	4	-0.03	0.02	0.04	-0.01	-	-
	5	-	-0.05	-0.05	0.02	-0.04	-
	6	-	-	-0.1	-0.01	0.04	-0.05
	7	-	-	-	0.08	0.17	0.13
	8	-	-	-	-	0.2	0.28
	9	-	-	-	-	-	0.33
Soil moisture	1	0.94	-	-	-	-	-
	2	-0.65	-0.08	-	-	-	-
	3	-0.24	-0.28	-0.39	-	-	-
	4	0.04	0.08	-0.04	-0.32	-	-
	5	-	0.03	0.14	-0.02	-0.27	-
	6	-	-	0.08	0	-0.05	-0.17
	7	-	-	-	0.19	-0.06	-0.06
	8	-	-	-	-	0.18	-0.11
	9	-	-	-	-	-	0.03
SEA	1	-0.06	-	-	-	-	-
	2	-0.01	-0.04	-	-	-	-
	3	-0.14	-0.12	-0.13	-	-	-
	4	-0.11	-0.14	-0.14	-0.17	-	-
	5	-	0.17	0.2	0.24	0.18	-
	6	-	-	0.03	0.08	0.13	0.14
	7	-	-	-	0.01	0.04	0
	8	-	-	-	-	0.04	0.04
	9	-	-	-	-	-	-0.1
NWMED SST	1	2.1	-	-	-	-	-
	2	-1.67	3.05	-	-	-	-
	3	-0.2	-3.31	1.99	-	-	-
	4	0.31	0.4	-2.37	1.35	-	-
	5	-	0.46	0.12	-2.5	0.46	-
	6	-	-	0.69	1.52	-1.09	-0.35
	7	-	-	-	-0.02	1.45	0.98
	8	-	-	-	-	-0.56	-0.23
	9	-	-	-	-	-	-0.26
CNAASST	1	-1.74	-	-	-	-	-
	2	1.8	-3.24	-	-	-	-
	3	0.36	3.67	-3.27	-	-	-
	4	-0.39	0.47	3.25	-4.15	-	-
	5	-	-1	2.04	7.83	-0.97	-
	6	-	-	-2.16	-4.93	2.34	1.38
	7	-	-	-	1.08	-3.27	-3.73
	8	-	-	-	-	1.74	3.05
	9	-	-	-	-	-	-0.76

734 TABLE D1. Regression coefficients for a single RR model trained on the full training set. Coefficients with

735 absolute values above 0.5 are bold.

Lead time		1 week		2 weeks		3 weeks		4 weeks		5 weeks		6 weeks	
Target		+1 σ	+1.5 σ	+1 σ	+1.5 σ	+1 σ	+1.5 σ	+1 σ	+1.5 σ	+1 σ	+1.5 σ	+1 σ	+1.5 σ
Predictor	Lag (weeks)												
Temperature	1	0.16	0.09	-	-	-	-	-	-	-	-	-	-
	2	-0.13	-0.06	-0.1	-0.03	-	-	-	-	-	-	-	-
	3	-0.05	-0.08	-0.13	-0.12	-0.11	-0.09	-	-	-	-	-	-
	4	-0.06	-0.03	-0.07	-0.04	-0.1	-0.06	-0.11	-0.07	-	-	-	-
	5	-	-	0.06	0.05	0.07	0.06	0.05	0.05	0.04	0.04	-	-
	6	-	-	-	-	0.07	0.04	0.09	0.07	0.07	0.06	0.07	0.06
	7	-	-	-	-	-	-	-0.03	-0.09	-0.01	-0.08	0	-0.07
	8	-	-	-	-	-	-	-	-	-0.01	-0.02	0.03	0.01
	9	-	-	-	-	-	-	-	-	-	-	-0.09	-0.08
Geopotential	1	-0.02	-0.04	-	-	-	-	-	-	-	-	-	-
	2	0.09	0.06	0.08	0.05	-	-	-	-	-	-	-	-
	3	0.02	0.07	0.08	0.1	0.06	0.09	-	-	-	-	-	-
	4	0.01	-0.01	0.02	-0.01	0.04	0.01	0.04	0.01	-	-	-	-
	5	-	-	-0.05	-0.03	-0.06	-0.02	-0.04	-0.02	-0.07	-0.03	-	-
	6	-	-	-	-	-0.04	-0.04	-0.06	-0.06	-0.04	-0.06	-0.04	-0.05
	7	-	-	-	-	-	-	0.03	0.05	-0.02	0.03	-0.04	0.02
	8	-	-	-	-	-	-	-	-	0.06	0.04	0.04	0.03
	9	-	-	-	-	-	-	-	-	-	-	0.12	0.08
Precipitation	1	-0.19	-0.1	-	-	-	-	-	-	-	-	-	-
	2	-0.01	-0.03	0.04	0.01	-	-	-	-	-	-	-	-
	3	0	0	0.02	0.02	0.03	0.04	-	-	-	-	-	-
	4	-0.01	0	-0.02	0	-0.01	0.01	-0.01	0.01	-	-	-	-
	5	-	-	-0.02	0	-0.02	-0.02	-0.01	-0.01	0	-0.01	-	-
	6	-	-	-	-	-0.02	-0.02	-0.01	-0.01	0.01	0	-0.02	-0.02
	7	-	-	-	-	-	-	0.03	0	0.07	0.02	0.05	0.01
	8	-	-	-	-	-	-	-	-	0.08	0.03	0.09	0.03
	9	-	-	-	-	-	-	-	-	-	-	0.15	0.07
Soil moisture	1	0.29	0.16	-	-	-	-	-	-	-	-	-	-
	2	-0.17	0	0	0.08	-	-	-	-	-	-	-	-
	3	-0.01	-0.05	-0.02	-0.06	-0.04	-0.02	-	-	-	-	-	-
	4	-0.02	-0.05	0.03	-0.05	0	-0.05	-0.04	-0.07	-	-	-	-
	5	-	-	-0.01	0.02	0.01	0.07	0	0.05	-0.06	-0.02	-	-
	6	-	-	-	-	0.03	-0.02	0	0	0	-0.01	-0.01	0
	7	-	-	-	-	-	-	0.02	0	-0.08	-0.04	-0.08	-0.04
	8	-	-	-	-	-	-	-	-	0.08	0.04	0.04	0.04
	9	-	-	-	-	-	-	-	-	-	-	-0.06	-0.04
SEA	1	-0.07	-0.03	-	-	-	-	-	-	-	-	-	-
	2	-0.03	-0.01	-0.03	-0.01	-	-	-	-	-	-	-	-
	3	-0.07	-0.04	-0.05	-0.03	-0.05	-0.03	-	-	-	-	-	-
	4	-0.06	-0.03	-0.07	-0.03	-0.06	-0.03	-0.06	-0.03	-	-	-	-
	5	-	-	0.05	0.02	0.05	0.03	0.06	0.03	0.04	0.02	-	-
	6	-	-	-	-	0.03	0.02	0.04	0.03	0.06	0.03	0.06	0.04
	7	-	-	-	-	-	-	0	-0.01	0.01	-0.01	0	-0.02
	8	-	-	-	-	-	-	-	-	0.01	0.02	0.02	0.02
	9	-	-	-	-	-	-	-	-	-	-	-0.02	-0.03
NWMED SST	1	0.66	0.37	-	-	-	-	-	-	-	-	-	-
	2	-0.71	-0.29	0.7	0.47	-	-	-	-	-	-	-	-
	3	0.25	0.01	-0.66	-0.54	0.46	0.25	-	-	-	-	-	-
	4	-0.04	0.01	-0.02	0.14	-0.39	-0.23	0.49	0.25	-	-	-	-
	5	-	-	0.15	0.02	-0.32	-0.11	-0.9	-0.43	0.16	0.03	-	-
	6	-	-	-	-	0.38	0.15	0.41	0.21	-0.39	0.03	-0.09	0.08
	7	-	-	-	-	-	-	0.11	0.02	0.34	-0.12	0.15	-0.08
	8	-	-	-	-	-	-	-	-	-0.03	0.12	0.01	-0.03
	9	-	-	-	-	-	-	-	-	-	-	-0.02	0.08
CNA A SST	1	-0.18	0	-	-	-	-	-	-	-	-	-	-
	2	0.54	0.09	-0.45	-0.24	-	-	-	-	-	-	-	-
	3	-0.29	-0.05	0.4	0.18	-0.67	-0.42	-	-	-	-	-	-
	4	0.02	-0.01	0.25	0.19	0.25	0.23	-1.55	-0.73	-	-	-	-
	5	-	-	-0.16	-0.12	1.17	0.58	2.8	1.3	-0.52	-0.18	-	-
	6	-	-	-	-	-0.75	-0.4	-1.53	-0.67	0.97	0.18	0.12	-0.12
	7	-	-	-	-	-	-	0.27	0.09	-0.66	0.03	-0.25	0.11
	8	-	-	-	-	-	-	-	-	0.2	-0.05	0.21	0.08
	9	-	-	-	-	-	-	-	-	-	-	-0.06	-0.08

736 TABLE D2. Regression coefficients for a single RC model trained on the full training set. Coefficients with
737 absolute values above 0.5 are bold.

Lead time		1 week	2 weeks	3 weeks	4 weeks	5 weeks	6 weeks
Predictor	Lag (weeks)						
Temperature	1	0.02	-	-	-	-	-
	2	0.01	0.03	-	-	-	-
	3	0.01	0.02	0.01	-	-	-
	4	0.01	0.05	0.03	0.01	-	-
	5	-	0.01	0	0.01	0.01	-
	6	-	-	0.01	0.02	0.02	0.02
	7	-	-	-	0.03	0.03	0.01
	8	-	-	-	-	0.01	0.01
	9	-	-	-	-	-	0.01
Geopotential	1	0.23	-	-	-	-	-
	2	0.01	0.01	-	-	-	-
	3	0.01	0	0	-	-	-
	4	0.01	0.01	0.01	0	-	-
	5	-	0	0.01	0.01	0.01	-
	6	-	-	0	0.01	0.01	0
	7	-	-	-	0.02	0.02	0.01
	8	-	-	-	-	0.01	0
	9	-	-	-	-	-	0.01
Precipitation	1	0.18	-	-	-	-	-
	2	0.03	0.01	-	-	-	-
	3	0.01	0.01	0.01	-	-	-
	4	0	0	0	0.01	-	-
	5	-	0	0	0.01	0.01	-
	6	-	-	0.01	0.02	0.02	0.02
	7	-	-	-	0.01	0	0.01
	8	-	-	-	-	0.01	0.01
	9	-	-	-	-	-	0.02
Soil moisture	1	0.01	-	-	-	-	-
	2	0.01	0.02	-	-	-	-
	3	0.01	0.02	0.02	-	-	-
	4	0.02	0.01	0.02	0.02	-	-
	5	-	0.04	0.05	0.04	0.05	-
	6	-	-	0.05	0.05	0.05	0.06
	7	-	-	-	0.01	0.01	0.01
	8	-	-	-	-	0.02	0.04
	9	-	-	-	-	-	0.03
SEA	1	0.07	-	-	-	-	-
	2	0.01	0.03	-	-	-	-
	3	0.01	0.01	0.03	-	-	-
	4	0.01	0.02	0.01	0.02	-	-
	5	-	0.06	0.08	0.06	0.05	-
	6	-	-	0.04	0.02	0.02	0.04
	7	-	-	-	0.03	0.03	0.04
	8	-	-	-	-	0.01	0.02
	9	-	-	-	-	-	0.01
NWMED SST	1	0.21	-	-	-	-	-
	2	0.01	0.35	-	-	-	-
	3	0.03	0.05	0.13	-	-	-
	4	0.01	0.03	0.03	0.07	-	-
	5	-	0.01	0.04	0.04	0.05	-
	6	-	-	0.06	0.04	0.05	0.05
	7	-	-	-	0.12	0.1	0.07
	8	-	-	-	-	0.04	0.04
	9	-	-	-	-	-	0.05
CNAASST	1	0.02	-	-	-	-	-
	2	0.02	0.1	-	-	-	-
	3	0.01	0.01	0.12	-	-	-
	4	0.02	0.03	0.03	0.06	-	-
	5	-	0.09	0.07	0.1	0.13	-
	6	-	-	0.12	0.15	0.16	0.23
	7	-	-	-	0.03	0.02	0.01
	8	-	-	-	-	0.07	0.02
	9	-	-	-	-	-	0.16

738 TABLE D3. Predictor importances for a single RFR model trained on the full training set. Values above
739 0.04 are bold.

Lead time		1 week		2 weeks		3 weeks		4 weeks		5 weeks		6 weeks	
Target		+1 σ	+1.5 σ	+1 σ	+1.5 σ	+1 σ	+1.5 σ	+1 σ	+1.5 σ	+1 σ	+1.5 σ	+1 σ	+1.5 σ
Predictor	Lag (weeks)												
Temperature	1	0.06	0.08	-	-	-	-	-	-	-	-	-	-
	2	0.02	0.02	0.03	0.02	-	-	-	-	-	-	-	-
	3	0.03	0.03	0.02	0.03	0.03	0.02	-	-	-	-	-	-
	4	0.03	0.03	0.03	0.03	0.03	0.03	0.03	0.03	0.03	-	-	-
	5	-	-	0.03	0.03	0.03	0.03	0.03	0.03	0.03	0.03	0.03	-
	6	-	-	-	-	0.03	0.02	0.03	0.02	0.03	0.02	0.03	0.02
	7	-	-	-	-	-	-	0.03	0.04	0.03	0.04	0.03	0.04
	8	-	-	-	-	-	-	-	-	0.03	0.03	0.03	0.03
	9	-	-	-	-	-	-	-	-	-	-	0.03	0.03
Geopotential	1	0.06	0.06	-	-	-	-	-	-	-	-	-	-
	2	0.02	0.02	0.03	0.03	-	-	-	-	-	-	-	-
	3	0.02	0.02	0.02	0.02	0.02	0.02	-	-	-	-	-	-
	4	0.02	0.02	0.03	0.03	0.03	0.02	0.03	0.02	-	-	-	-
	5	-	-	0.03	0.03	0.03	0.03	0.03	0.02	0.03	0.02	-	-
	6	-	-	-	-	0.03	0.02	0.03	0.02	0.02	0.02	0.03	0.03
	7	-	-	-	-	-	-	0.03	0.03	0.03	0.03	0.03	0.03
	8	-	-	-	-	-	-	-	-	0.03	0.03	0.03	0.02
	9	-	-	-	-	-	-	-	-	-	-	0.02	0.03
Precipitation	1	0.07	0.06	-	-	-	-	-	-	-	-	-	-
	2	0.02	0.02	0.03	0.03	-	-	-	-	-	-	-	-
	3	0.02	0.02	0.02	0.02	0.02	0.03	-	-	-	-	-	-
	4	0.02	0.02	0.02	0.02	0.02	0.02	0.02	0.03	-	-	-	-
	5	-	-	0.03	0.03	0.02	0.03	0.02	0.02	0.02	0.02	-	-
	6	-	-	-	-	0.03	0.02	0.03	0.02	0.03	0.02	0.03	0.02
	7	-	-	-	-	-	-	0.03	0.02	0.02	0.02	0.02	0.02
	8	-	-	-	-	-	-	-	-	0.02	0.03	0.02	0.03
	9	-	-	-	-	-	-	-	-	-	-	0.03	0.03
Soil moisture	1	0.03	0.03	-	-	-	-	-	-	-	-	-	-
	2	0.03	0.04	0.03	0.04	-	-	-	-	-	-	-	-
	3	0.03	0.02	0.03	0.03	0.03	0.03	-	-	-	-	-	-
	4	0.03	0.03	0.03	0.03	0.03	0.03	0.03	0.03	-	-	-	-
	5	-	-	0.04	0.04	0.04	0.04	0.04	0.05	0.04	0.05	-	-
	6	-	-	-	-	0.04	0.04	0.04	0.03	0.04	0.03	0.04	0.03
	7	-	-	-	-	-	-	0.03	0.03	0.03	0.03	0.03	0.03
	8	-	-	-	-	-	-	-	-	0.03	0.03	0.04	0.03
	9	-	-	-	-	-	-	-	-	-	-	0.03	0.03
SEA	1	0.05	0.06	-	-	-	-	-	-	-	-	-	-
	2	0.03	0.03	0.04	0.04	-	-	-	-	-	-	-	-
	3	0.03	0.04	0.04	0.05	0.04	0.05	-	-	-	-	-	-
	4	0.03	0.03	0.03	0.04	0.03	0.04	0.04	0.04	-	-	-	-
	5	-	-	0.04	0.04	0.04	0.04	0.03	0.04	0.04	0.04	-	-
	6	-	-	-	-	0.04	0.04	0.03	0.03	0.03	0.04	0.03	0.03
	7	-	-	-	-	-	-	0.03	0.03	0.03	0.02	0.03	0.03
	8	-	-	-	-	-	-	-	-	0.03	0.03	0.03	0.03
	9	-	-	-	-	-	-	-	-	-	-	0.03	0.04
NWMED SST	1	0.06	0.08	-	-	-	-	-	-	-	-	-	-
	2	0.04	0.04	0.06	0.07	-	-	-	-	-	-	-	-
	3	0.04	0.04	0.05	0.05	0.05	0.06	-	-	-	-	-	-
	4	0.03	0.03	0.04	0.04	0.05	0.04	0.05	0.04	-	-	-	-
	5	-	-	0.05	0.04	0.04	0.04	0.04	0.04	0.05	0.04	-	-
	6	-	-	-	-	0.05	0.05	0.04	0.05	0.04	0.05	0.04	0.05
	7	-	-	-	-	-	-	0.04	0.05	0.04	0.05	0.04	0.05
	8	-	-	-	-	-	-	-	-	0.05	0.04	0.04	0.04
	9	-	-	-	-	-	-	-	-	-	-	0.05	0.06
CNAASST	1	0.04	0.03	-	-	-	-	-	-	-	-	-	-
	2	0.04	0.03	0.06	0.04	-	-	-	-	-	-	-	-
	3	0.04	0.03	0.04	0.04	0.05	0.04	-	-	-	-	-	-
	4	0.04	0.03	0.05	0.04	0.05	0.04	0.05	0.04	-	-	-	-
	5	-	-	0.06	0.05	0.06	0.06	0.06	0.06	0.07	0.06	-	-
	6	-	-	-	-	0.06	0.06	0.06	0.06	0.06	0.06	0.07	0.05
	7	-	-	-	-	-	-	0.05	0.06	0.05	0.06	0.05	0.05
	8	-	-	-	-	-	-	-	-	0.05	0.05	0.05	0.05
	9	-	-	-	-	-	-	-	-	-	-	0.06	0.05

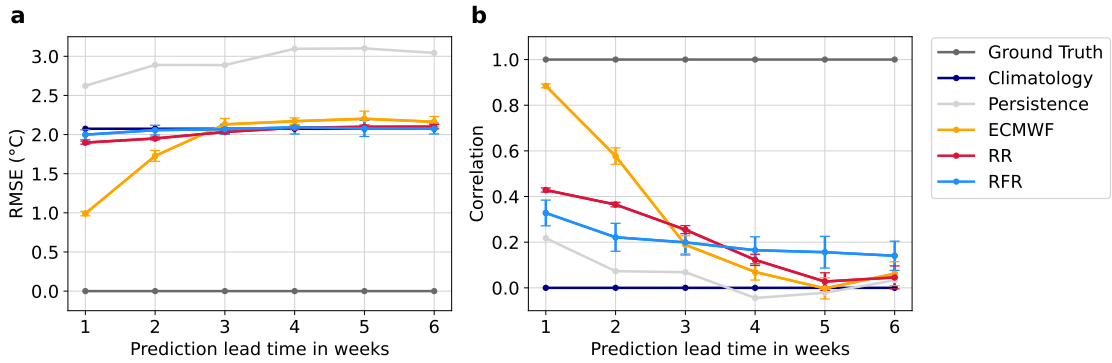
740 TABLE D4. Predictor importances for a single RFC model trained on the full training set. Values above
741 0.04 are bold.

742

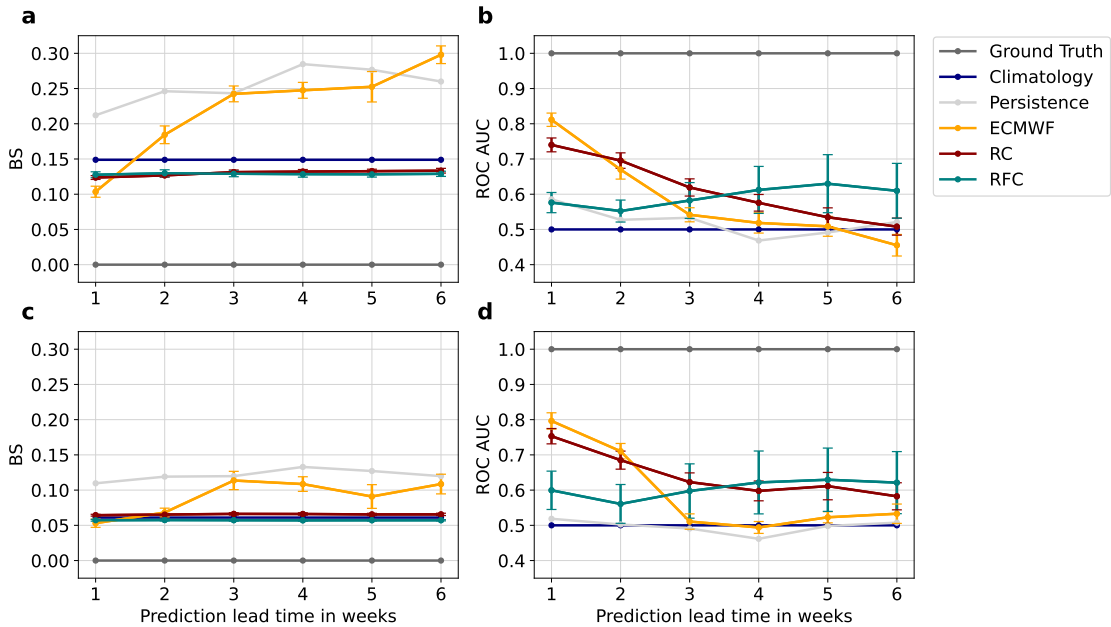
APPENDIX E

743

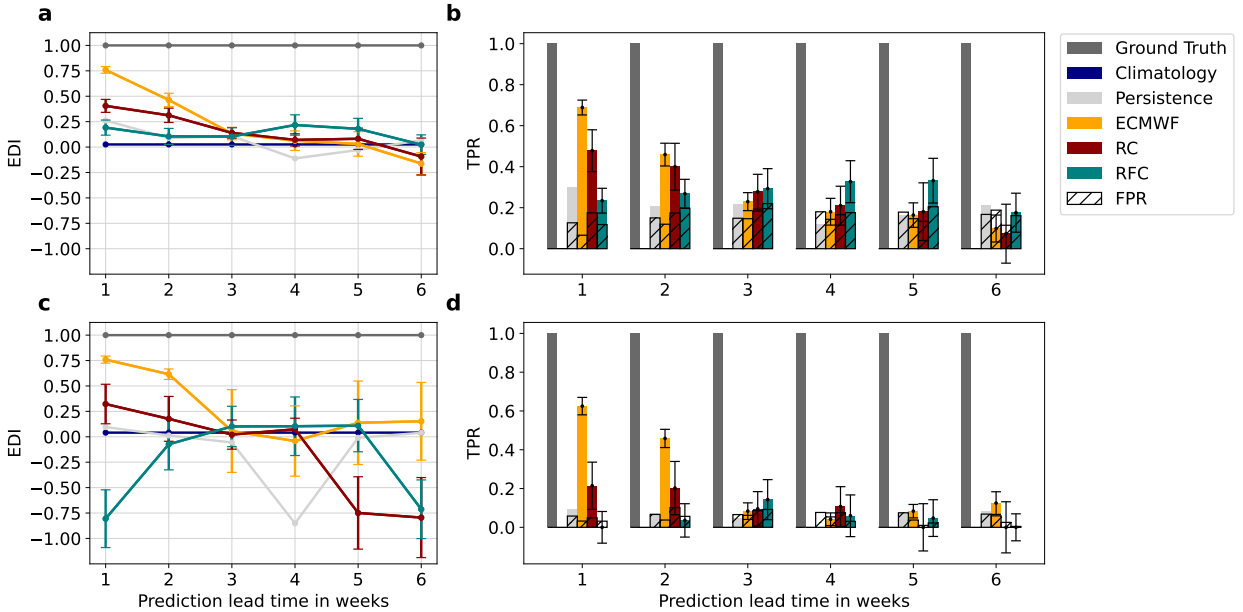
Only-SST runs



744 FIG. E1. Performance of the regression models for six different lead times using only the *NWMED*
745 and *CNA A SST* predictors. (a) RMSE and (b) correlation for the regression forecasts. An accurate forecast
746 is characterized by a low RMSE and a high correlation. The error bars show the uncertainty of each forecast
747 estimated via the standard deviation of the ensemble.



748 FIG. E2. Performance of the probabilistic classification models for six different lead times using only the
 749 *NWMED* and *CNA SST* predictors. BS and ROC AUC for the $+1\sigma$ (a&b) and $+1.5\sigma$ (c&d) weekly heatwave
 750 indices. An accurate probabilistic classification forecast is characterized by a low BS and a high ROC AUC. A
 751 no-skill probabilistic classification forecast is represented by a BS of 1 and a ROC AUC of 0.5 (as indicated by
 752 the climatology). The error bars show the uncertainty of each forecast estimated via the standard deviation of
 753 the ensemble.



754 **FIG. E3. Performance of the binary classification models for six different lead times using only the**
 755 ***NWMed* and *CNAASST* predictors.** (a) EDI and (b) TPR (coloured bars) and FPR (stippled bars) for the $+1\sigma$
 756 weekly heatwave index. (c) and (d) are the corresponding forecasts for the $+1.5\sigma$ weekly heatwave index. An
 757 accurate binary classification forecast is characterized by a high EDI, a high TPR, and a low FPR. The error bars
 758 show the uncertainty of each forecast estimated via the standard deviation of the ensemble. Since the climatology
 759 forecast predicts only zeros (no heatwave), both its TPR and FPR are equal to zero at all lead times (Figs. b&d).

760 **References**

- 761 Barriopedro, D., E. M. Fischer, J. Luterbacher, R. M. Trigo, and R. Garcia-Herrera, 2011: The
762 hot summer of 2010: Redrawing the temperature record map of europe. *Science*, **332**, 220–224,
763 <https://doi.org/10.1126/science.1201224>.
- 764 Bassil, K., and D. Cole, 2010: Effectiveness of public health interventions in reducing morbidity
765 and mortality during heat episodes: a structured review. *International Journal of Environmental*
766 *Research and Public Health*, **7**, 991–1001, <https://doi.org/10.3390/ijerph7030991>.
- 767 Basu, R., 2002: Relation between elevated ambient temperature and mortality: a review of the
768 epidemiologic evidence. *Epidemiologic Reviews*, **24**, 190–202, <https://doi.org/10.1093/epirev/mxf007>.
- 770 Black, E., M. Blackburn, G. Harrison, B. Hoskins, and J. Methven, 2004: Factors contributing to
771 the summer 2003 european heatwave. *Weather*, **59**, 217–223, <https://doi.org/10.1256/wea.74.04>.
- 772 Bladé, I., B. Liebmann, D. Fortuny, and G. J. van Oldenborgh, 2011: Observed and simulated
773 impacts of the summer nao in europe: Implications for projected drying in the mediterranean
774 region. *Climate Dynamics*, **39**, 709–727, <https://doi.org/10.1007/s00382-011-1195-x>.
- 775 Bradley, A. P., 1997: The use of the area under the roc curve in the evaluation of machine learn-
776 ing algorithms. *Pattern Recognition*, **30**, 1145–1159, [https://doi.org/10.1016/s0031-3203\(96\)](https://doi.org/10.1016/s0031-3203(96)00142-2)
777 [00142-2](https://doi.org/10.1016/s0031-3203(96)00142-2).
- 778 Breiman, L., 2001: Random forests. *Machine Learning*, **45**, 5–32, [https://doi.org/10.1023/a:](https://doi.org/10.1023/a:1010933404324)
779 [1010933404324](https://doi.org/10.1023/a:1010933404324).
- 780 Buzan, J. R., and M. Huber, 2020: Moist heat stress on a hotter earth. *Annual Review of Earth and*
781 *Planetary Sciences*, **48**, <https://doi.org/10.1146/annurev-earth-053018-060100>.
- 782 Casanueva, A., and Coauthors, 2019: Overview of existing heat-health warning systems in europe.
783 *International Journal of Environmental Research and Public Health*, **16**, [https://doi.org/10.](https://doi.org/10.3390/ijerph16152657)
784 [3390/ijerph16152657](https://doi.org/10.3390/ijerph16152657).

- 785 Chattopadhyay, A., E. Nabizadeh, and P. Hassanzadeh, 2020: Analog forecasting of extreme-
786 causing weather patterns using deep learning. *Journal of Advances in Modeling Earth Systems*,
787 **12**, <https://doi.org/10.1029/2019ms001958>.
- 788 Cornes, R. C., G. van der Schrier, E. J. M. van den Besselaar, and P. D. Jones, 2018: An ensemble
789 version of the e-obs temperature and precipitation data sets. *Journal of Geophysical Research:*
790 *Atmospheres*, **123**, 9391–9409, <https://doi.org/10.1029/2017jd028200>.
- 791 de Perez, E. C., and Coauthors, 2018: Global predictability of temperature extremes. *Environmental*
792 *Research Letters*, **13**, 1748–9318, <https://doi.org/10.1088/1748-9326/aab94a>.
- 793 Deb, P., H. Moradkhani, P. Abbaszadeh, A. S. Kiem, J. Engström, D. Keellings, and A. Sharma,
794 2020: Causes of the widespread 2019–2020 australian bushfire season. *Earth's Future*, **8**, 2328–
795 4277, <https://doi.org/10.1029/2020ef001671>.
- 796 Dee, D. P., and Coauthors, 2011: The era-interim reanalysis: configuration and performance of the
797 data assimilation system. *Quarterly Journal of the Royal Meteorological Society*, **137**, 553–597,
798 <https://doi.org/10.1002/qj.828>.
- 799 Duchez, A., and Coauthors, 2016: Drivers of exceptionally cold north atlantic ocean temper-
800 atures and their link to the 2015 european heat wave. *Environmental Research Letters*, **11**,
801 <https://doi.org/10.1088/1748-9326/11/7/074004>.
- 802 Ferro, C. A. T., and D. B. Stephenson, 2011: Extremal dependence indices: Improved verification
803 measures for deterministic forecasts of rare binary events. *Weather and Forecasting*, **26**, 699–713,
804 <https://doi.org/10.1175/waf-d-10-05030.1>.
- 805 Fischer, E. M., S. I. Seneviratne, P. L. Vidale, D. Lüthi, and C. Schär, 2007: Soil mois-
806 ture–atmosphere interactions during the 2003 european summer heat wave. *J. Climate*, **20**,
807 5081–5099, <https://doi.org/10.1175/jcli4288.1>.
- 808 Folland, C. K., J. Knight, H. W. Linderholm, D. Fereday, S. Ineson, and J. W. Hurrell, 2009: The
809 summer north atlantic oscillation: Past, present, and future. *Journal of Climate*, **22**, 1082–1103,
810 <https://doi.org/10.1175/2008jcli2459.1>.

811 Ford, T. W., P. A. Dirmeyer, and D. O. Benson, 2018: Evaluation of heat wave forecasts seamlessly
812 across subseasonal timescales. *Npj Climate and Atmospheric Science*, **1**, [https://doi.org/10.1038/](https://doi.org/10.1038/s41612-018-0027-7)
813 [s41612-018-0027-7](https://doi.org/10.1038/s41612-018-0027-7).

814 Gneiting, T., F. Balabdaoui, and A. E. Raftery, 2007: Probabilistic forecasts, calibration and
815 sharpness. *Journal of the Royal Statistical Society: Series B (Statistical Methodology)*, **69**,
816 243–268, <https://doi.org/10.1111/j.1467-9868.2007.00587.x>.

817 Haiden, T., M. Janousek, F. Vitart, Z. B. Bouallegue, L. Ferranti, F. Prates, and D. Richardson,
818 2019: Technical memorandum: Evaluation of ecmwf forecasts, including the 2019 upgrade.
819 10.21957/mlvapkke, URL <https://www.ecmwf.int/node/19277>.

820 Hastie, T., R. Tibshirani, and J. Friedman, 2009: *The Elements of Statistical learning: Data*
821 *mining, inference, and Prediction*. 2nd ed., Springer, 61–68, 249–254, and 587–588 pp.

822 Hersbach, H., and Coauthors, 2020: The era5 global reanalysis. *Quarterly Journal of the Royal*
823 *Meteorological Society*, **146**, 1999–2049, <https://doi.org/10.1002/qj.3803>.

824 Hu, Z.-Z., A. Kumar, B. Huang, W. Wang, J. Zhu, and C. Wen, 2012: Prediction skill of monthly
825 sst in the north atlantic ocean in ncep climate forecast system version 2. *Climate Dynamics*, **40**,
826 2745–2759, <https://doi.org/10.1007/s00382-012-1431-z>.

827 Huynen, M. M., P. Martens, D. Schram, M. P. Weijenberg, and A. E. Kunst, 2001: The impact
828 of heat waves and cold spells on mortality rates in the dutch population. *Environmental Health*
829 *Perspectives*, **109**, 463–470, <https://doi.org/10.1289/ehp.01109463>.

830 IPCC, 2013: *Climate Change 2013 - The Physical Science Basis Working Group I Contribution to*
831 *the Fifth Assessment Report of the Intergovernmental Panel on Climate Change*, Vol. Chapter 9:
832 Evaluation of Climate Models. Cambridge University Press, 768 pp.

833 Jacques-Dumas, V., F. Ragone, P. Borgnat, P. Abry, and F. Bouchet, 2022: Deep learning-based
834 extreme heatwave forecast. *Frontiers in Climate*, **4**, <https://doi.org/10.3389/fclim.2022.789641>.

835 Jiménez-Esteve, B., and D. I. Domeisen, 2022: The role of atmospheric dynamics and large-scale
836 topography in driving heatwaves. *Quarterly Journal of the Royal Meteorological Society*, **148**,
837 2344–2367, <https://doi.org/10.1002/qj.4306>.

- 838 Jolliffe, I. T., and D. B. Stephenson, 2005: Comments on “discussion of verification concepts in
839 forecast verification: A practitioner’s guide in atmospheric science”. *Weather and Forecasting*,
840 **20**, 796–800, <https://doi.org/10.1175/waf877.1>.
- 841 Kautz, L.-A., O. Martius, S. Pfahl, J. G. Pinto, A. M. Ramos, P. M. Sousa, and T. Woollings, 2022:
842 Atmospheric blocking and weather extremes over the euro-atlantic sector – a review. *Weather
843 and Climate Dynamics*, **3**, 305–336, <https://doi.org/10.5194/wcd-3-305-2022>.
- 844 Khan, N., S. Shahid, L. Juneng, K. Ahmed, T. Ismail, and N. Nawaz, 2019: Prediction of heat waves
845 in pakistan using quantile regression forests. *Atmospheric Research*, **221**, 1–11, [https://doi.org/
846 10.1016/j.atmosres.2019.01.024](https://doi.org/10.1016/j.atmosres.2019.01.024).
- 847 Kolstad, E. W., E. A. Barnes, and S. P. Sobolowski, 2017: Quantifying the role of land-atmosphere
848 feedbacks in mediating near-surface temperature persistence. *Quarterly Journal of the Royal
849 Meteorological Society*, **143**, 1620–1631, <https://doi.org/10.1002/qj.3033>.
- 850 Kotharkar, R., and A. Ghosh, 2022: Progress in extreme heat management and warning systems:
851 A systematic review of heat-health action plans (1995-2020). *Sustainable Cities and Society*, **76**,
852 <https://doi.org/10.1016/j.scs.2021.103487>.
- 853 Kumar, A., and J. Zhu, 2018: Spatial variability in seasonal prediction skill of ssts: Inherent
854 predictability or forecast errors? *Journal of Climate*, **31**, 613–621, [https://doi.org/10.1175/
855 jcli-d-17-0279.1](https://doi.org/10.1175/jcli-d-17-0279.1).
- 856 Kunsch, H. R., 1989: The jackknife and the bootstrap for general stationary observations. *The
857 Annals of Statistics*, **17**, <https://doi.org/10.1214/aos/1176347265>.
- 858 Kämäräinen, M., P. Uotila, A. Y. Karpechko, O. Hyvärinen, I. Lehtonen, and J. Räisänen, 2019:
859 Statistical learning methods as a basis for skillful seasonal temperature forecasts in europe. *J.
860 Climate*, **32**, 5363–5379, <https://doi.org/10.1175/jcli-d-18-0765.1>.
- 861 Laguë, M. M., G. B. Bonan, and A. L. S. Swann, 2019: Separating the impact of indi-
862 vidual land surface properties on the terrestrial surface energy budget in both the coupled
863 and uncoupled land–atmosphere system. *Journal of Climate*, **32**, 5725–5744, [https://doi.org/
864 10.1175/jcli-d-18-0812.1](https://doi.org/10.1175/jcli-d-18-0812.1).

- 865 Lemaitre, G., F. Nogueira, and C. K. Aridas, 2017: Imbalanced-learn: a python toolbox to tackle
866 the curse of imbalanced datasets in machine learning. *Journal of Machine Learning Research*,
867 **18**, 1–5, <https://doi.org/10.1175/mwr-d-14-00277.1>.
- 868 Li, S., and A. W. Robertson, 2015: Evaluation of submonthly precipitation forecast skill from
869 global ensemble prediction systems. *Monthly Weather Review*, **143**, 2871–2889, <https://doi.org/10.1175/mwr-d-14-00277.1>.
- 871 Lopez-Gomez, I., A. McGovern, S. Agrawal, and J. Hickey, 2022: Global extreme heat forecasting
872 using neural weather models. *arXiv*, <https://doi.org/10.48550/ARXIV.2205.10972>.
- 873 Lowe, D., K. L. Ebi, and B. Forsberg, 2011: Heatwave early warning systems and adaptation advice
874 to reduce human health consequences of heatwaves. *International Journal of Environmental
875 Research and Public Health*, **8**, 4623–4648, <https://doi.org/10.3390/ijerph8124623>.
- 876 Manrique-Suñén, A., N. Gonzalez-Reviriego, V. Torralba, N. Cortesi, and F. J. Doblas-Reyes,
877 2020: Choices in the verification of s2s forecasts and their implications for climate services.
878 *Monthly Weather Review*, **148**, 3995–4008, <https://doi.org/10.1175/mwr-d-20-0067.1>.
- 879 Manzanas, R., 2020: Assessment of model drifts in seasonal forecasting: Sensitivity to ensemble
880 size and implications for bias correction. *Journal of Advances in Modeling Earth Systems*, **12**,
881 <https://doi.org/10.1029/2019ms001751>.
- 882 Mecking, J. V., S. S. Drijfhout, J. J.-M. Hirschi, and A. T. Blaker, 2019: Ocean and atmosphere
883 influence on the 2015 european heatwave. *Environmental Research Letters*, **14**, <https://doi.org/10.1088/1748-9326/ab4d33>.
- 885 Mehta, P., M. Bukov, C.-H. Wang, A. G. Day, C. Richardson, C. K. Fisher, and D. J. Schwab, 2019:
886 A high-bias, low-variance introduction to machine learning for physicists. *Physics Reports*, **810**,
887 1–124, <https://doi.org/10.1016/j.physrep.2019.03.001>.
- 888 Menze, B. H., B. M. Kelm, R. Masuch, U. Himmelreich, P. Bachert, W. Petrich, and F. A. Ham-
889 precht, 2009: A comparison of random forest and its gini importance with standard chemometric
890 methods for the feature selection and classification of spectral data. *BMC Bioinformatics*, **10**,
891 213, <https://doi.org/10.1186/1471-2105-10-213>.

- 892 Merz, B., and Coauthors, 2020: Impact forecasting to support emergency management of natural
893 hazards. *Reviews of Geophysics*, **58**, 8755–1209, <https://doi.org/10.1029/2020rg000704>.
- 894 Miller, D. E., Z. Wang, B. Li, D. S. Harnos, and T. Ford, 2021: Skillful subseasonal prediction
895 of united states extreme warm days and standardized precipitation index in boreal summer.
896 *Journal of Climate, American Meteorological Society*, **34**, 5887–5898, [https://doi.org/10.1175/
897 jcli-d-20-0878.1](https://doi.org/10.1175/jcli-d-20-0878.1).
- 898 Molteni, F., T. Stockdale, and M. Balmaseda, 2011: The new ecmwf seasonal forecast system
899 (system 4). *ECMWF Technical Memoranda*, **656**, 35, <https://doi.org/10.21957/4nery093i>.
- 900 Mueller, B., and S. I. Seneviratne, 2012: Hot days induced by precipitation deficits at the global
901 scale. *Proceedings of the National Academy of Sciences*, **109**, 12 398–12 403, [https://doi.org/
902 10.1073/pnas.1204330109](https://doi.org/10.1073/pnas.1204330109).
- 903 Murphy, A. H., 1993: What is a good forecast? an essay on the nature of goodness in weather
904 forecasting. *Wea. Forecasting*, **8**, 281–293, [https://doi.org/10.1175/1520-0434\(1993\)008<0281:
905 wiagfa>2.0.co;2](https://doi.org/10.1175/1520-0434(1993)008<0281:wiagfa>2.0.co;2).
- 906 Muñoz-Sabater, J., and Coauthors, 2021: Era5-land: a state-of-the-art global reanalysis
907 dataset for land applications. *Earth System Science Data*, **13**, 4349–4383, [https://doi.org/
908 10.5194/essd-13-4349-2021](https://doi.org/10.5194/essd-13-4349-2021).
- 909 Nembrini, S., I. R. König, and M. N. Wright, 2018: The revival of the gini importance?
910 *Bioinformatics*, **34**, 3711–3718, <https://doi.org/10.1093/bioinformatics/bty373>, URL [https:
911 //repository.publisso.de/resource/fri:6411640/data](https://repository.publisso.de/resource/fri:6411640/data).
- 912 Oliveira, J. C., E. Zorita, V. Koul, T. Ludwig, and J. Baehr, 2020: Forecast opportunities for
913 european summer climate ensemble predictions using self-organising maps. *Proceedings of the
914 10th International Conference on Climate Informatics*, 67–71, [https://doi.org/10.1145/3429309.
915 3429319](https://doi.org/10.1145/3429309.3429319).
- 916 Ossó, A., R. Sutton, L. Shaffrey, and B. Dong, 2020: Development, amplification, and decay of at-
917 lantic/european summer weather patterns linked to spring north atlantic sea surface temperatures.
918 *J. Climate*, **33**, 5939–5951, <https://doi.org/10.1175/JCLI-D-19-0613.1>.

- 919 Pedregosa, F., and Coauthors, 2011: Scikit-learn: Machine learning in python. *Journal of Machine*
920 *Learning Research*, **12**, 2825–2830, <https://doi.org/arXiv:1201.0490>, URL [https://scikit-learn.](https://scikit-learn.org/stable/)
921 [org/stable/](https://scikit-learn.org/stable/).
- 922 Perkins, S. E., 2015: A review on the scientific understanding of heatwaves -their measurement,
923 driving mechanisms, and changes at the global scale. *Atmospheric Research*, **164–165**, 242–267,
924 <https://doi.org/10.1016/j.atmosres.2015.05.014>.
- 925 Perkins, S. E., and L. V. Alexander, 2013: On the measurement of heat waves. *J. Climate*, **26**,
926 4500–4517, <https://doi.org/10.1175/jcli-d-12-00383.1>.
- 927 Perkins-Kirkpatrick, S. E., and S. C. Lewis, 2020: Increasing trends in regional heatwaves. *Nature*
928 *Communications*, **11**, <https://doi.org/10.1038/s41467-020-16970-7>.
- 929 Pyrina, M., M. Nonnenmacher, S. Wagner, and E. Zorita, 2021: Statistical seasonal prediction of
930 european summer mean temperature using observational, reanalysis and satellite data. *Weather*
931 *and Forecasting*, **36**, <https://doi.org/10.1175/waf-d-20-0235.1>.
- 932 Rasp, S., and N. Thuerey, 2021: Data-driven medium-range weather prediction with a resnet
933 pretrained on climate simulations: A new model for weatherbench. *Journal of Advances in*
934 *Modeling Earth Systems*, **13**, 1942–2466, <https://doi.org/10.1029/2020ms002405>.
- 935 Rayner, N. A., D. E. Parker, E. B. Horton, C. K. Folland, L. V. Alexander, D. P. Rowell, E. C. Kent,
936 and A. Kaplan, 2003: Global analyses of sea surface temperature, sea ice, and night marine air
937 temperature since the late nineteenth century. *Journal of Geophysical Research*, **108**, 148–227,
938 <https://doi.org/10.1029/2002jd002670>.
- 939 Reichstein, M., G. Camps-Valls, B. Stevens, M. Jung, J. Denzler, and N. Carvalhais, 2019: Deep
940 learning and process understanding for data-driven earth system science. *Nature*, **566**, 195–204,
941 <https://doi.org/10.1038/s41586-019-0912-1>.
- 942 Robertson, A. W., A. Kumar, M. Peña, and F. Vitart, 2015: Improving and promoting sub-
943 seasonal to seasonal prediction. *Bull. Amer. Meteor. Soc.*, **96**, ES49–ES53, [https://doi.org/](https://doi.org/10.1175/bams-d-14-00139.1)
944 [10.1175/bams-d-14-00139.1](https://doi.org/10.1175/bams-d-14-00139.1).

- 945 Rudin, C., 2019: Stop explaining black box machine learning models for high stakes decisions
946 and use interpretable models instead. *Nature Machine Intelligence*, **1**, 206–215, [https://doi.org/](https://doi.org/10.1038/s42256-019-0048-x)
947 10.1038/s42256-019-0048-x.
- 948 Runge, J., P. Nowack, M. Kretschmer, S. Flaxman, and D. Sejdinovic, 2019: Detecting and
949 quantifying causal associations in large non-linear time series datasets. *Science Advances*, **5**,
950 eaau4996, <https://doi.org/10.1126/sciadv.aau4996>.
- 951 Schwingshackl, C., M. Hirschi, and S. I. Seneviratne, 2017: Quantifying spatiotemporal variations
952 of soil moisture control on surface energy balance and near-surface air temperature. *Journal of*
953 *Climate*, **30**, 7105–7124, <https://doi.org/10.1175/jcli-d-16-0727.1>.
- 954 Seneviratne, S. I., T. Corti, E. L. Davin, M. Hirschi, E. B. Jaeger, I. Lehner, B. Orlowsky, and A. J.
955 Teuling, 2010: Investigating soil moisture–climate interactions in a changing climate: a review.
956 *Earth-Science Reviews*, **99**, 125–161, <https://doi.org/10.1016/j.earscirev.2010.02.004>.
- 957 Seneviratne, S. I., M. G. Donat, B. Mueller, and L. V. Alexander, 2014: No pause in the increase
958 of hot temperature extremes. *Nature Climate Change*, **4**, 161–163, [https://doi.org/10.1038/](https://doi.org/10.1038/nclimate2145)
959 nclimate2145.
- 960 Smola, A. J., P. L. Bartlett, B. Schölkopf, and D. Schuurmans, 2000: *Probabilities for SVMachines*,
961 61–75. *Advances in Large Margin Classifiers*, The MIT Press.
- 962 Sobhani, N., D. del Vento, and A. Fanfarillo, 2018: Long-lead forecast of heatwaves in the eastern
963 united states using artificial intelligence. *Proceedings of the Amer. Geophysical Union, Fall*
964 *Meeting 2018*.
- 965 Spensberger, C., and Coauthors, 2020: Dynamics of concurrent and sequential central european
966 and scandinavian heatwaves. *Quarterly Journal of the Royal Meteorological Society*, **146**, 2998–
967 3013, <https://doi.org/10.1002/qj.3822>.
- 968 Steyerberg, E. W., A. J. Vickers, N. R. Cook, T. Gerds, M. Gonen, N. Obuchowski, M. J. Pencina,
969 and M. W. Kattan, 2010: Assessing the performance of prediction models. *Epidemiology*, **21**,
970 128–138, <https://doi.org/10.1097/ede.0b013e3181c30fb2>.
- 971 Storch, H. V., and F. W. Zwiers, 2003: *Statistical analysis in climate research*. Cambridge Univer-
972 sity Press, 293–299 pp.

973 Suarez-Gutierrez, L., W. A. Mueller, C. Li, and J. Marotzke, 2020: Dynamical and thermodynamical drivers of variability in european summer heat extremes. *Climate Dynamics*, **54**, 4351–4366, <https://doi.org/10.1007/s00382-020-05233-2>.

974

975

976 Vabalas, A., E. Gowen, E. Poliakoff, and A. J. Casson, 2019: Machine learning algorithm validation with a limited sample size. *PLOS ONE*, **14**, <https://doi.org/10.1371/journal.pone.0224365>.

977

978 van Straaten, C., K. Whan, D. Coumou, B. van den Hurk, and M. Schmeits, 2022: Using explainable machine learning forecasts to discover sub-seasonal drivers of high summer temperatures in western and central europe. *Mon. Wea. Rev.*, <https://doi.org/10.1175/mwr-d-21-0201.1>.

979

980

981 Vijverberg, S., M. Schmeits, K. van der Wiel, and D. Coumou, 2020: Subseasonal statistical forecasts of eastern u.s. hot temperature events. *Mon. Wea. Rev.*, **148**, 4799–4822, <https://doi.org/10.1175/mwr-d-19-0409.1>.

982

983

984 Vitart, F., 2014: Evolution of ecmwf sub-seasonal forecast skill scores. *Quarterly Journal of the Royal Meteorological Society*, **140**, 1889–1899, <https://doi.org/10.1002/qj.2256>.

985

986 Wallemacq, P., R. Below, and D. McClean, 2018: Economic losses, poverty and disasters (1998–2017). URL <https://www.undrr.org/publication/economic-losses-poverty-disasters-1998-2017>, 1–9 pp.

987

988

989 Weyn, J. A., D. R. Durran, and R. Caruana, 2019: Can machines learn to predict weather? using deep learning to predict gridded 500-hpa geopotential height from historical weather data. *Journal of Advances in Modeling Earth Systems*, **11**, 2680–2693, <https://doi.org/10.1029/2019ms001705>.

990

991

992

993 Wheeler, M. C., H. Zhu, A. H. Sobel, D. Hudson, and F. Vitart, 2016: Seamless precipitation prediction skill comparison between two global models. *Quarterly Journal of the Royal Meteorological Society*, **143**, 374–383, <https://doi.org/10.1002/qj.2928>.

994

995

996 White, C. J., and Coauthors, 2017: Potential applications of subseasonal-to-seasonal (s2s) predictions. *Meteorological Applications*, **24**, 315–325, <https://doi.org/10.1002/met.1654>.

997

998 White, C. J., and Coauthors, 2021: Advances in the application and utility of subseasonal-to-seasonal predictions. *Bull. Amer. Meteor. Soc.*, **aop**, 1–57, <https://doi.org/10.1175/bams-d-20-0224.1>.

999

1000

- 1001 Wilks, D. S., 2019: *Statistical Methods in the Atmospheric Sciences*. 4th ed., Elsevier, 379 and
1002 386–388 (Chapter 9) pp.
- 1003 Wulff, C. O., and D. I. V. Domeisen, 2019: Higher subseasonal predictability of extreme hot
1004 european summer temperatures as compared to average summers. *Geophysical Research Letters*,
1005 **46**, 11 520–11 529, <https://doi.org/10.1029/2019gl084314>.
- 1006 Wulff, C. O., R. J. Greatbatch, D. I. V. Domeisen, G. Gollan, and F. Hansen, 2017: Tropical forcing
1007 of the summer east atlantic pattern. *Geophysical Research Letters*, **44**, 94–8276, [https://doi.org/](https://doi.org/10.1002/2017gl075493)
1008 [10.1002/2017gl075493](https://doi.org/10.1002/2017gl075493).
- 1009 Wunderlich, R. F., Y.-P. Lin, J. Anthony, and J. R. Petway, 2019: Two alternative evaluation
1010 metrics to replace the true skill statistic in the assessment of species distribution models. *Nature*
1011 *Conservation*, **35**, 97–116, <https://doi.org/10.3897/natureconservation.35.33918>.
- 1012 Zheng, X., and C. S. Frederiksen, 2007: Statistical prediction of seasonal mean southern
1013 hemisphere 500-hpa geopotential heights. *Journal of Climate*, **20**, 2791–2809, [https://doi.org/](https://doi.org/10.1175/jcli4180.1)
1014 [10.1175/jcli4180.1](https://doi.org/10.1175/jcli4180.1).
- 1015 Zuo, J., H.-L. Ren, J. Wu, Y. Nie, and Q. Li, 2016: Subseasonal variability and predictability of
1016 the arctic oscillation/north atlantic oscillation in bcc_agcm2.2. *Dynamics of Atmospheres and*
1017 *Oceans*, **75**, 33–45, <https://doi.org/10.1016/j.dynatmoce.2016.05.002>.